25th AIAA Applied Aerodynamics Conference
June 25–28, 2007/Miami, FL

Validation Study of Aerodynamic Analysis Tools for Design Optimization of Helicopter Rotors

Seongim Choi*, Juan J. Alonso†, Edwin v.d. Weide‡
Stanford University, Stanford, CA 94305

Jaina Sitaraman§
National Institute of Aerospace, Hampton, , VA 23666

The key objectives of this paper are to assess the accuracy and the validity of our current aerodynamic analysis tools in predicting the unsteady flow field generated by helicopter rotors and to investigate their applicability to the future design problems. A Reynolds-Averaged Naiver-Stokes (RANS) solver with various turbulence models has been used with necessary modifications for the computation of all test cases. Dynamic stall and massive separation, which are physical phenomena characteristic of helicopter flows, are analyzed first using RANS methodology, and Detached Eddy Simulation (DES) is applied to the simulation of massive separation and compared to corresponding RANS solutions. The periodic nature of the helicopter flowfield strongly motivates the application of Time-Spectral (TS) approach for unsteady RANS computations. In this paper, the TS method is applied to simulate actual flight conditions of the UH-60A helicopter and is verified to be a fast and efficient algorithm which maintains the same level of accuracy as the time-accurate approach. In addition, the TS method also provides great potential for adjoint based design optimization of helicopter rotors as the governing equations can be reduced to a periodic steady state.

I. Introduction

Design optimization of helicopter rotors has been a main focus of research in the military and industry for a long time. However, the level of its complexity is higher than for other types of vehicles, as the problem is inherently coupled with structural dynamics, controls and acoustics. Therefore, the design optimization of helicopter rotors require a multi-disciplinary approach, where the accuracy of each discipline plays a critical role in the success of the overall procedure. From an aerodynamic analysis viewpoint, the associated difficulties are numerous. Massive separation occurs at bluff structures such as pylons, rotor hubs and fuselage contributing to the large increase in the pressure drag. The blades on the retreating side of the rotor suffer momentum loss from the onset of dynamic stall in forward flight, and the advancing side experiences transonic flow and associate shock formation. The vortex wakes generated from the rotating blade tips interact with the other blades, often resulting large fluctuations in the aerodynamic loading and a highly turbulent flow field. Therefore, the use of high-fidelity analysis tools becomes critical since the complex flow phenomena remain unresolved when using simple lower-fidelity tools.[1] Although modern high performance computing facilities become more available, the use of high-fidelity analysis tools for three-dimensional full rotor configuration still remains a challenge. Therefore the development of accurate but computationally inexpensive analysis tools would produce substantial benefits in the design process.

*Research Associate, AIAA Member
†Associate Professor, AIAA Member
‡Research Associate, AIAA Member
§Research Scientist, AIAA Member

Reynold Averaged Navier Stokes (RANS) equations have been widely used in various engineering applications because of the relatively inexpensive computational cost. In the RANS approach, the Navier-Stokes equations through time-averaging process. Closure of the Navier-Stokes eqution are achieved by utilizing turbulence models which provide the effects of flow fluctuations within their own assumptions. Although RANS computation is highly efficient, its accuracy is often limited when the details of the turbulent flows are solved. Direct numerical simulation (DNS) or Large eddy simulation (LES) can resolve the small scale features of the turbulent flows by attempting to directly solve the governing equations without using time-averaging process or turbulence modeling. However, corresponding computational expense is enormous demanding a huge computing resources. In contrast to DNS, LES introduces sub-grid scale model to approximate the small scale eddies to reduce this computational cost, and yet the requirement of high mesh resolution and the restriction of Reynolds numbers make its application to the helicopter problem still challenging.

Detached eddy simulation (DES) was proposed as a hybrid technique by combining the aforementioned two flow solution methods (RANS and LES) in 1997 by Spalart et al[21] and has been successfully applied to a variety of engineering problems.[3,4] This approach benefits from the favorable aspects of both methods by applying RANS mode to the near wall region and LES mode to the region away from the wall. The justification comes from the fact that RANS can resolve the flow properties relatively well within the boundary layer where turbulent length scale is smaller than the maximum grid dimension, and LES can directly solve large scale turbulent eddies in the regions where detached separation takes place. DES has a number of advantages over pure RANS or LES of less strict requirements of the mesh size and Reynolds number, simplicity in implementation, and a reasonable computational cost. In this paper, both approaches, RANS and DES, are employed to investigate their capabilities to simulate the flow phenomena often encountered in a helicopter flight; dynamic stall of pitching airfoils and massive separation around the bluff body components. Various turbulence models including one, two and four equation models are tested in the context of RANS computations.

As computation extends from two- to three-dimension for the complete simulation of a helicopter flight, corresponding computational cost increases dramatically. The simulation requires a computational domain large enough to capture the interactions between vortex wakes and the blades , and a time-accurate computation should be performed to simulate the unsteady flow involved. Recently Time-Spectral (TS) method[27–29,32] has been proposed as an efficient algorithm for the simulation of unsteady periodic flows. It has been applied to a large number of applications such as turbine, turbomachinery, and flapping wings. Helicoper flows are apporpriate candiates for application of the TS method owing to their periodic nature. However not many studies have been devoted to investigating this possiblity as yet. The TS method represents the periodic time response of the flow as Fourier modes/basis and does not require transient computation to reach periodic steady-state. The idea of Fourier representation in time for the unsteady periodic flow has been explored in the past, and there have been some attempts[25,26] to solve the governing equations in the frequency-domain and transform back to the time-domain to obtain the physical interpretation of the flow solutions. TS method differs from the conventional frequency domain methods and offers more advantages. It solves the governing equations directly in the time-domain and thus removes the process of transforming the flow solutions between the frequency- and time-domain. This also makes the problem of the implementation of the algorithm more straightforward. Another significant benefit of using TS method is that the gradient sensitivities of the flow solutions become much easier to obtain since their dependence on the time evolution is eliminated. Fourier representation of a time derivative term in the governing equations reduces their unsteady formulation to that of the steady-state simulation. This fact becomes very critical when we integrate the flow analysis module into a design optimization procedure. A well-known competent adjoint solution method can be easily implemented for the steady-state form of the governing equations otherwise unsteady adjoint formulation should be applied for time-accurate unsteady computation. Therefore the use of TS method provides great potentials for the future design optimization problems in addition to the savings of computational cost for a flow analysis.

Followings are the test cases that are studied in this paper to verify and validate the accuracy of the analysis tools:

- Dynamic stall of pitching airfoils (NACA0015 and SC1095) is simulated using RANS computations. Aerodynamic forces of C_l, C_d, and C_m are plotted corresponding to various turbulence models and compared with wind-tunnel experiments.

- Flows around NACA0036 airfoil at three fixed angles of attack ($\alpha = 0°, 5°, 10°$) are simulated to

examine the similarities and differences in the capabilities of RANS and DES methods to capture the flow properties when the flow experiences from moderate to massive separation.

- Finally three critical flight conditions for the UH-60A configuration, consisting of high speed level flight (case 8534), low speed transition (case 8515) and high altitude stall (case 9017), are simulated with both the time-accurate and the TS methods. The results from TS method show good agreement with time-accurate computations for all the test cases but at much reduced cost. The amount of cost savings and the additional memory requirements for TS method will be also discussed.

This paper is organized as follows. The details of the different flow solution techniques will be explained in Section II. Results of three validation studies, dynamic stall prediction, massive separation simulation, and UH-60A flight test simulation, will be shown in Section III.A, III.B, and III.C respectively. Conclusions and future work of our validation studies are presented at Section IV

II. Flow Solution Method

A. Reynolds-Averaged Navier-Stokes Simulation (RANS)

RANS has been popular and widely used for a large number of engineering applications across various fields because of its comparatively inexpensive computational cost. RANS gives approximated averaged solutions to the Navier-Stokes equations by the method of Reynolds-averaging,[9] which involves separation of the instantaneous flow variable into the mean component and the fluctuating component as follows.

$$\rho\frac{\partial U_i}{\partial t}+\rho U_j\frac{\partial U_i}{\partial x_j}=-\frac{\partial P}{\partial x_i}+\frac{\partial}{\partial x_j}\left(2\mu S_{ji}-\rho\overline{u_j'u_i'}\right), \tag{1}$$

where the capital letters stand for time-averaged (mean) properties, and the small letters for fluctuating parts. The quantity $-\rho\overline{u_i'u_j'}$ is the Reynolds-stress tensor, and the way of solving this quantity characterizes various turbulence models. The main advantage of RANS is its efficiency in computation by solving for mean flow properties only. However, this fact at the same time causes the limitations when detailed information about turbulent structures are necessary.

Three-dimensional compressible Navier-Stokes flow solver, SUmb (Stanford University multi-block), has been utilized for all computations in this paper. SUmb is a multi-block structured flow solver developed at Stanford University under the sponsorship of the Department of Energy Advanced Strategic Computing (ASC) program. Various turbulence models are implemented to capture the viscous and turbulent properties of the flow: Baldwin-Lomax, Spalart-Allmaras, $k-\omega$, Menter SST, v^2-f. Details of each turbulent model can be found in References,[7,9,10,12,13,15] and only their distinctive characteristics will be summarized below. SUmb is a massively parallel code (in both CPU and memory) using scalable pre-processor, load balancing, and MPI. It employs multigrid, Runge-Kutta time stepping for the mean flow, and DD-ADI solution methodology for the turbulence equations. Central difference discretization (second order in space) with several artificial dissipation options (scalar or matrix), or upwind discretization is available for a space discretization. For unsteady time integration, second-/third-order backwards difference formula(BDF) or the time-spectral approach for time-periodic flows can be used, which will be explained in detail in Section II.B. SUmb has been successfully used in many applications including simulation of launch vehicles, space and re-entry vehicles, jet/turbo engines, subsonic and supersonic aircraft, and helicopters.

1. *Turbulence Modeling*

One- and two-equation models such as Spalart-Allmaras (S-A), $k-\epsilon$, Wilcox's original and modified $k-\omega$, Menter's SST models are available inside SUmb. These models are based on the Boussinesq linear eddy-viscosity hypothesis, but the main differences lie in the way of computing the turbulence length scale or its equivalent. Two- equation models include the transport equations of the variables such as the turbulent kinetic energy (k), the dissipation of turbulent kinetic energy per unit mass (ϵ), and the specific dissipation rate (ω). A modified production term by Kato-Launder formula is also available to circumvent the tendency of over-predicting turbulent production in regions with strong acceleration or deceleration. The use of wall-function[14] was available to add the damping effects to the near-wall regions and to improve the capability to predict the velocity profile in the logarithmic layer near a wall.

On the other hand, four-equation turbulence model, first proposed by P.Durbin,[13] has proven to be successful in analyzing such cases as three-dimensional turbulent boundary layer and heat transfer. It eliminates the necessity of wall- or damping-function by introducing the transport equation of the velocity fluctuation normal to the surface ($\overline{v^2}$). A well-known near-wall non-local effects of the pressure-deformation fluctuations was reproduced by adding the elliptic-relaxation equation for the pressure-strain term (f). The main advantages of $v^2 - f$ turbulence model are 1) it automatically reflects the blocking effect of the solid boundary by solving the equations of $\overline{v^2}$ and f with the proper boundary conditions. The eddy viscosity is calculated from $\overline{v^2}$, and 2) anisotropic turbulent properties near wall is accounted for by adding the local anisotropy term in the ϵ equation.

Modifications to the original $v^2 - f$ turbulence model were recently suggested[15,17] to better simulate the tip vorticies trailing downstream from the wing/blade tips. Turbulence level in the vortical core of the trailing vortices is shown to be largely reduced[18] due to the near-solid body rotation existing in the inner core. Thus non-inertial and streamline curvature effect was added in the original $v^2 - f$ turbulence model to reflect. Both turbulence models, the original $v^2 - f$ and the modified $v^2 - f$ model, are used for our computation, and the results are compared with one- and two-equation models

Detailed explanation of each turbulence model can be found in References,[7–10] and the turbulence models employed for our analysis are following.

- Spalart-Allmars[7,8]
- $k - \omega$ [9]
- Menter's SST[10]
- $v^2 - f$ [12,13]
- $v^2 - f$ with curvature corrections[15,17]

B. Detached Eddy Simulation (DES)

While RANS simulation is greatly appreciated for its efficiency, its simplicity related to the approximation of the mean properties of the flow has restricted its application to the simulation of highly turbulent flows often induced by massive separation. DNS attempts to resolve all scales of turbulent structures ranging from the smallest dissipative scales up to the integral scales associated with main flow motion. However, it is well-known that the method is not feasible for the problems involving complex geometries as it requires correspondingly high mesh resolution, a large computation domain, and high order numerical methods. LES seeks to decrease the computational cost by solving the only large scales of turbulent eddies and modeling the small scale eddies. The grounds of this modeling comes from the famous Kolmogorov's theory of self-similarity where small scale eddies have rather universal characteristics and easily modeled. A computational mesh for LES thus needs to be fine only enough to capture large scale turbulent structures, which enables the method less expensive than DNS. However the level of required mesh resolution in the vicinity of the wall increases dramatically ($\sim Re^2$)[19] limiting its application to the simulation of the flow with high Reynolds number which is typical of the analysis of helicopter rotors.

Recently a number of efforts to combine RANS and LES have been made to relieve this computational burden such as the integration of the proper wall models into LES[20] and zonal coupling of RANS and LES.[30] DES[21] has been proposed as one of these hybrid techniques and was designed to simulate massively separated flows. The method uses nonzonal approach to apply both methods to the computational domain in an integrated way. In the region near solid boundaries where the size of the turbulent structure is small, turbulence models of RANS can resolve the flow properties relatively well. For a region where massive separation occurs and turbulent length scale exceeds the local grid dimension, DES switches the dominant length scale of the flow to the local grid size, and the simulation resembles the sub-grid scale approximation of LES. This makes DES more true to reality as the destruction term in various turbulence models is often inversely proportional to the wall distance($\sim 1/d^2$ in S-A model), which causes very little dissipation far away from the wall boundary. This is not physically accurate considering the dissipative properties of turbulent structures, and a wall distance can no longer contribute to predicting the dissipation of turbulent structures. The introduction of a more realistic wall distance based on the local grid size can solve this problem.

A more detailed description for S-A model based DES is referred to References[21] and the brief outline is given here. A production term for the eddy viscosity $\tilde{\nu}$ in original S-A model is proportional to $(\tilde{\nu}/d)^2$,

where $\tilde{\nu}$ stands for a eddy viscosity and d for a wall distance. Balanced by a production term, the eddy viscosity term becomes proportional to Sd^2 ($\tilde{\nu} \sim Sd^2$), where S represents the mean rate of strain tensor ($S_{ij} = 1/2(\frac{\partial U_i}{\partial x_j} + \frac{\partial U_j}{\partial x_i})$). We can infer from these relations that the original S-A model predicts lower destruction and higher production as the wall distance increases and thus can significantly under-predict the dissipation of the turbulent flows. On the other hand, the eddy viscosity term from SGS model in LES scales with $S\Delta^2$, where Δ is a local grid spacing. The concept of S-A model based DES is that if we switch d to Δ in the region where the original S-A model fails in predicting the eddy viscosity, and then it follows SGS model of LES.

The wall distance function in the S-A model, d, is replaced with a modified distance function, $\tilde{d}$, by the following mathematical formula,

$$\tilde{d} = \min(d, C_{DES}\Delta), \tag{2}$$

where C_{DES} is a constant and Δ is the largest dimension of the local grid cell in question. With the assumption of isotropic turbulent flows, C_{DES} is commonly chosen as 0.65.

$$\Delta = \max(\Delta x, \Delta y, \Delta z), \tag{3}$$

where $\Delta x, \Delta y$, and Δz are the grid spacing among the neighboring cells in each direction. In this way, the entire boundary layer where grid spacing normal to the wall is less than a boundary layer thickness ($d << \Delta$) is solved by S-A model, and a separated region detached away from the wall ($d >> \Delta$) is handled by sub-grid model. Unlike other zonal approaches to couple RANS and LES, DES employs the switching criteria based on the local grid size. As a result, an explicit additional effort to decouple the domains for RANS and DES is not necessary,and the variations of the flow variables across the interface regions remain smooth.

This concept is not difficult to implement and simple in nature, and it can be applied to various turbulence models. A similar approach is applied to Menter's SST model.[22] The turbulence length scale l obtained from the turbulent equations is compared with the local grid size to switch between RANS and LES. The only change in the SST model is in the source term in the k equation.

$$\tilde{l} = \min(l, C_{DES}\Delta) \tag{4}$$

The main advantage of DES is the savings in the mesh resolution near the wall which in pure LES is required to be fairly high for the simulation of the flows at high Reynolds numbers. Although computational cost is higher than RANS simulation alone, the improvement in accuracy is such that DES often can resolve the turbulent flow field RANS is not able to solve. However it should be noted that the accuracy and the efficieny of DES is substantially subject to the mesh topology. The construcution of the mesh with reasonable resolutions for RANS and LES simulation is an important issue for its sucess.

C. Time-Spectral Method

A simulation of helicopter flight inevitably entails the complete computation of three-dimensional rotor, and the corresponding computational cost grows rapidly in addition to the complexity related to the mesh construction. Therefore, the efficiency and the accuracy of the numerical scheme of URANS solver becomes very crucial. As the flows involved show unsteady periodic nature a second order implicit Backward Difference Formula has been successfully used for its merit of A-stability allowing larger time steps than those of explicit time-stepping method. A set of nonlinear equations for the new state are solved and advanced in time utilizing inner iterations involving dual time-stepping. Combined with several convergence acceleration techniques[23] including multigrid and implicit residual smoothing, its efficiency can be remarkably improved. However the computational cost of this methodology can still be considerably large when applied to the unsteady periodic simulations where at least two or three cycles (five or more for a pitching motion) should be preceded before it reaches periodic steady-state.

Fully taking the advantage of the periodic nature of the flow and based on the idea of Fourier series form of the periodic responses, Hall et.al.[24] proposed Harmonic balance techniques to transform the unsteady equations in the physical domain into a steady problem in the frequency domain. This approach has been extended as a non-linear frequency-domain (NLFD) method[24,25] to Euler and full Navier-Stokes equations and applied to a number of unsteady flow analyeis[25] and aerodynamic/aero-structural shape optimization.[26]

Compared to the time-accurate computations, NLFD method can achieve a higher efficiency by eliminating the cost to compute initial transient computation to reach the periodic steady-state. A mathematical formulations are given as follow.

The Navier-Stokes equations in a semi-discrete form in the Cartesian coordinates can be written as

$$V\frac{\partial \omega}{\partial t} + R(\omega) = 0 \ , \tag{5}$$

where ω is the vector of conservative variables,

$$\omega = \begin{pmatrix} \rho \\ \rho u \\ \rho v \\ \rho w \\ \rho E \end{pmatrix} \ , \tag{6}$$

and $R(\omega)$ is the residual of spatial discretizations of viscous, inviscid and numerical dissipation fluxes.

A discretization of Equation 5 using a pseudo-spectral formula[31] renders equations

$$VD_t\omega^n + R(\omega^n) = 0 \ (n = 0, 1, 2, ..., N-1) \ , \tag{7}$$

where N is the number of time intervals, and D_t is the spectral time derivative operator. If we apply a forward discrete Fourier transform[38] to Equation 5 and add the pseudo-time derivative term for time integration, then the corresponding NS equations to the one in the frequency-domain becomes

$$V\frac{d\hat{\omega}_k}{d\tau} + ikV\hat{\omega}_k + \hat{R}_k = 0 \ (k = -\frac{N}{2}, ..., 0, ...\frac{N}{2} - 1) \ , \tag{8}$$

where k is the wave numbers. The cost of solving Equation 8 is much less than its counter part in the time-domain, Equation 5, since it reduces the original unsteady equations to a steady-state form. However, the solutions we are interested in are in the physical time domain, and thus an inverse Fourier transform back into time-domain is required at each iteration, which makes the frequency-domain method less attractive.

On the other hand, in the same context of the NLFD method of the Fourier representation in time, Time-Spectral method has been proposed.[27] The main advantage of TS approach over the frequency-domain method lies in the efficiency in a computational cost. TS method represents the time derivative term in the NS equations as the Fourier series directly in the time-domain, and thus removes the process required in the frequency-domain method to transform the solutions back and forth to the time-domain. The algorithm of TS method is also more straightforward to implement in the NS equations. Details of the mathematical formulation and stability analysis are described in Reference,[27] and the only brief summary is shown here.

If a pseudo-time derivative term is directly added to Equation 7, then

$$V\frac{\partial \omega^n}{\partial \tau} + VD_t\omega^n + R(\omega^n) = 0 \ (n = 0, 1, 2, ..., N-1) \ . \tag{9}$$

Equation 9 takes on the inverse Fourier transform of Equation 8. Hence TS method can achieve the same level of stability of the frequency-domain method at a much reduced computational cost. The efficiency of TS method rises from the treatment of $D_t\omega^n$ term in Equation 9. Instead of transforming the equations into the frequency-domain, the inverse form of Fourier transform of the time derivative term in Equation 7 is

$$D_t\omega^n = \frac{2\pi}{T}\sum_{k=-\frac{N-1}{2}}^{k=\frac{N-1}{2}} ik\hat{\omega}_k e^{ikn\Delta t} \ (n = 0, 1, 2, ..., N-1), \tag{10}$$

where time period T is divided into N time intervals, $\Delta t = \frac{T}{N}$, and $\hat{\omega_k}$ is a Fourier mode. This can be rewritten in the time domain as suggested,[31]

$$D_t\omega^n = \frac{2\pi}{T}\sum_{m=-\frac{N-1}{2}}^{\frac{N-1}{2}} d_m\omega^{n+m} \ (n = 0, 1, 2, ..., N-1), \tag{11}$$

A term d_m can be rearranged as

$$d_m = \begin{cases} \frac{1}{2}(-1)^{m+1} cosec(\frac{\pi m)}{N}) & : m \neq 0 \\ 0 & : m = 0 \ . \end{cases} \tag{12}$$

Thus a time derivative term in Equation 9 behaves as a matrix operator, and an additional cost in TS method comes from the operation related to the multiplication of matrix with the elements d_m and the vector ω^{n+m} in Equation 12. The summation in Equation 11 involves the solutions at all time levels, and the solution at each time instance depends on the solutions at all other time instances. Thus the solution at each time instance is updated simultaneously as the computation advances in physical time-domain until desired convergence is achieved. This does increases the memory requirement of TS method as solutions at all time levels need to be stored. However, if the frequency contents of the problem we are simulating do not span a wide range of the spectrum, this method can considerably contribute to improving the efficiency at an accuracy equivalent to that of the time-accurate computations.

III. Results

A. Validation I: Prediction of Dynamic Stall of Pitching Airfoil (NACA0015 and SC1095)

As the first validation case, dynamic stalls of two pitching airfoils (NACA0015 & SC1095) are simulated using RANS with various turbulence models, and the results are compared with experimental data available from NASA.[34] The case of NACA0015 airfoil is shown first. Mach number is $M = 0.29$, and Reynolds number $Re = 1.951 \times 10^6$ based on the chord length. The reduced frequency is $F^+ = 0.096$, which amount to the natural frequency $\omega = 63.7$. A pitching amplitude is $\Delta\alpha = 4.16^o$, while the mean amplitude is $\alpha_o = 15^o$. The periodic pitching motion, $\alpha(t)$, is approximated by sine function, $\alpha(t) = \alpha_o + \Delta\alpha \cdot \sin\omega t$. The mesh topology for this calculation is shown in Figure 1. A C-type mesh is generated with 129 points along the wake region, 259 points in circumferential direction of the airfoil, and 129 points in the normal direction to the surface ($Y^+ \sim 1$).

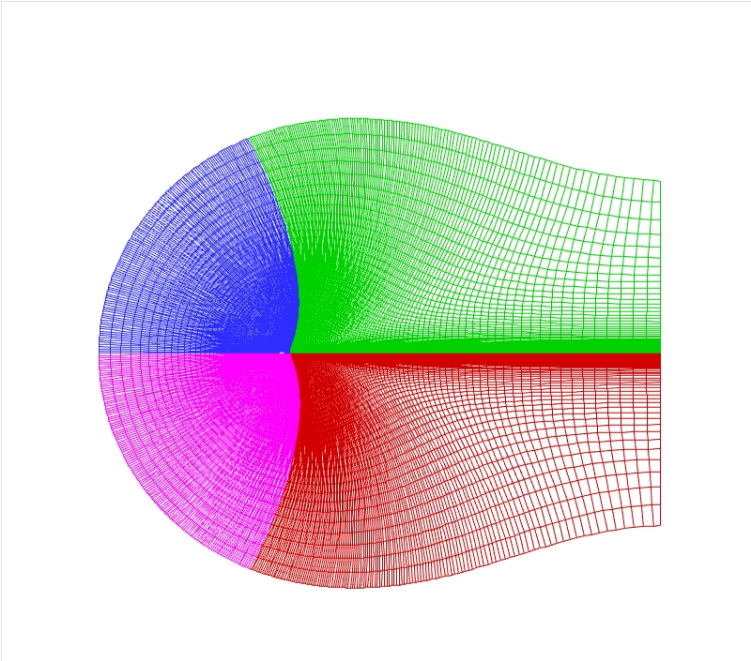

Figure 1. C-type mesh around NACA0015 airfoil

Computed aerodynamic forces (C_l, C_d, and C_m) are plotted in Figure 2 corresponding to each turbulence model, and compared with experimental data. It is difficult to conclude that any particular turbulence model shows the most accurate results for all three cases, however Menter's SST and the S-A model appear to show the best overall agreement for the dynamic stall simulation of the NACA0015 airfoil.

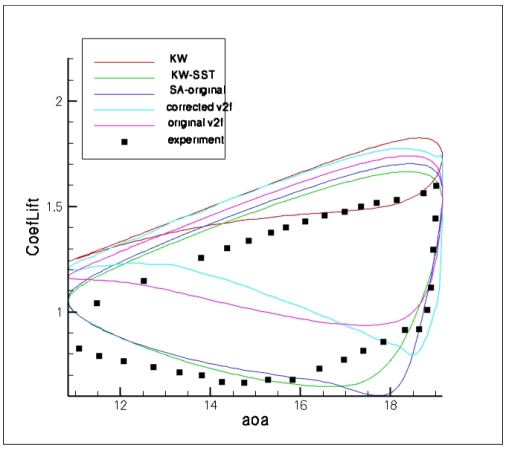

(a) Comparison of C_l

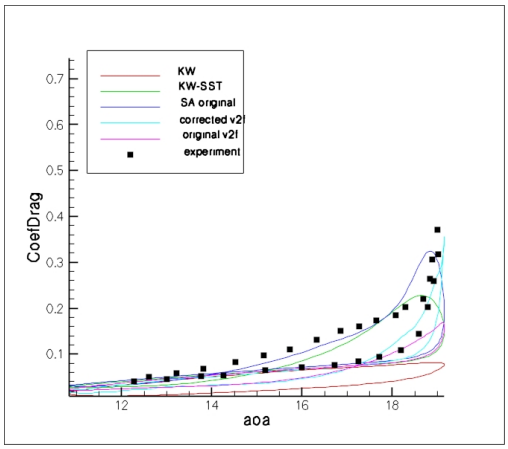

(b) Comparison of C_d

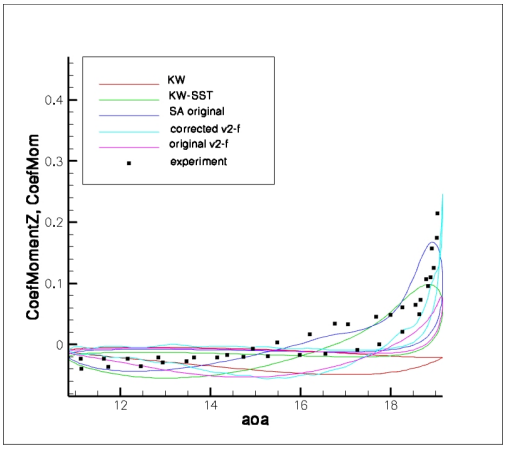

(c) Comparison of C_m

Figure 2. Comparison of aerodynamic forces using various turbulence modeling for NACA0015

A second simulation of two-dimensional dynamic stall was performed on SC1095 airfoil which is one of the airfoil sections utilized in the UH-60A rotor blade. The integrated investigations on the overall UH-60A flight conditions is discussed in detail in a later section. Again unsteady RANS simulation with different turbulence models was applied, and the resulting aerodynamic forces are shown in Figure 3. Although simulations at other angles of attack ($\alpha = 5^\circ$ and 15°) were conducted, the one at $\alpha = 10^\circ$ is presented in this paper as others show similar nature. Reduced frequency is $F^+ = 0.1$, Mach number is $M = 0.3$, and Reynolds number is $Re = 3.7 \times 10^6$. A Pitching motion is described as $\alpha(t) = 10 + 10\sin(\omega t)$. Results in Figure 3 show reasonable agreements with the experiments.

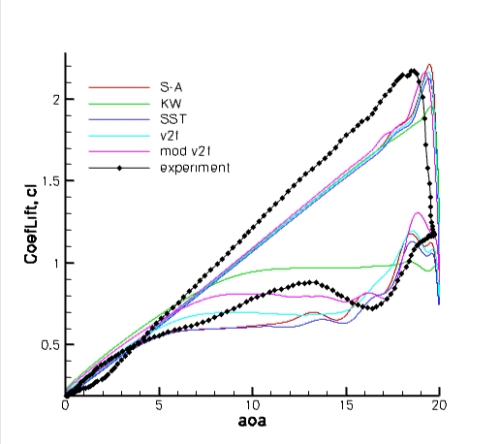

(a) Comparison of C_l

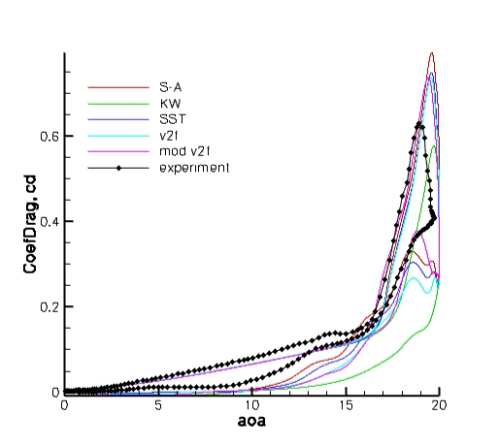

(b) Comparison of C_d

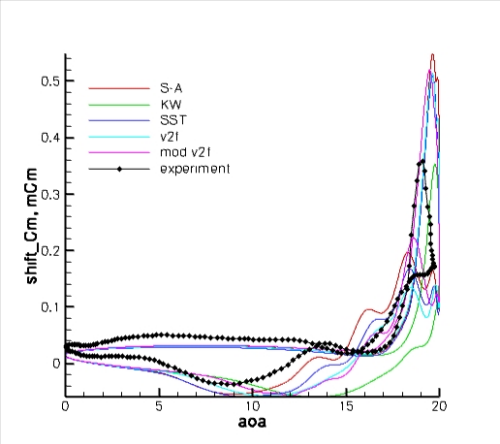

(c) Comparison of C_m

Figure 3. Effect of turbulence modeling on SC1095 2D dynamic stall prediction.

This second simulation of dynamic stall reaffirms the previous observation that a specific turbulence model which shows the best accuracy for all the cases is not evident. The simulation demonstrates little distinctive differences among the turbulence models with an exception of $k - \omega$ model which shows rather poor prediction of all. It is also noticeable that $v^2 - f$ model or $v^2 - f$ model with streamline curvature correction does not appear to improve to a large extent the accuracy of the simulation unlike the previous studies.[20] The high Reynolds number in this problem can be a reasonable explanation for this fact, and further research on that aspects is deemed necessary. A recent study[16] shows that the incorporation of a wall effect into a simulation by incorporating the bounded walls in the far-fields can enhance the accuracy of dynamic stall simulation significantly. A test with this suggestion is left for future work.

Based on the results from two simulations of dynamic stall and less computational costs involved, we will adopt S-A turbulence model for the validation studies in Section B and C.

B. Validation II: Massive Separation around NACA0036 airfoil

A second validation study is the prediction of massive separation around NACA0036 airfoil. As one of the active flow control methods to reduce the pressure drag caused by bluff-body components, synthetic jet blowing the potential to delay separation by adding momentum into the boundary layer.[2,5] Because of its thickness, NACA0036 airfoil is chosen to represent the bluff body components on the helicopter. The experiment was conducted in the NASA Ames Fluid Mechanics Laboratory $32inch \times 4ft$ wind tunnel.[2] Details of the experimental set-up can be found in in Reference.[2,5] The chord is $2ft$ long and the span is $4/3$ ft wide. Synthetic jet blowing is located at $x/c = 30\%$ and 65%. The flow conditions in the computation are set up such that they duplicate the experimental conditions. Reynolds number is $Re = 9 \times 10^5$ based on the chord length, and Mach number is $M = 0.0676$. the turbulence level in the freestream was set low and the initial turbulent eddy viscosity is assigned as 0.1%.

The mesh topology for computation is shown in Figure 4. Two simulation approaches, unsteady RANS computation and DES, are employed for comparison purposes. The S-A turbulence model and Menter's SST model were modified according to DES approach and are referred to as SA-DES and SST-DES respectively in this paper. RANS simulation uses a two-dimensional mesh topology, and 573 points were placed in the circumferential direction of the airfoil and 129 points in the wall normal direction. As DES requires a three-dimensional mesh topology, a total of 64 grid cells were uniformly spaced in the spanwise direction with the periodic boundary conditions imposed at the ends. Beacause mesh resolution in the RANS region and LES region is critical to the accuracy of DES, the mesh was carefully generated corresponding to the guideline.[33] The mesh is clustered around four locations of the jet blowing slots to better resolve the detailed flow properties around jet blowing, and is shown in Figure 4(b) Although the simulation of a flow control case with actual synthetic jet blowing can be conducted, only a baseline configuration without jet blowing is considered in this paper.

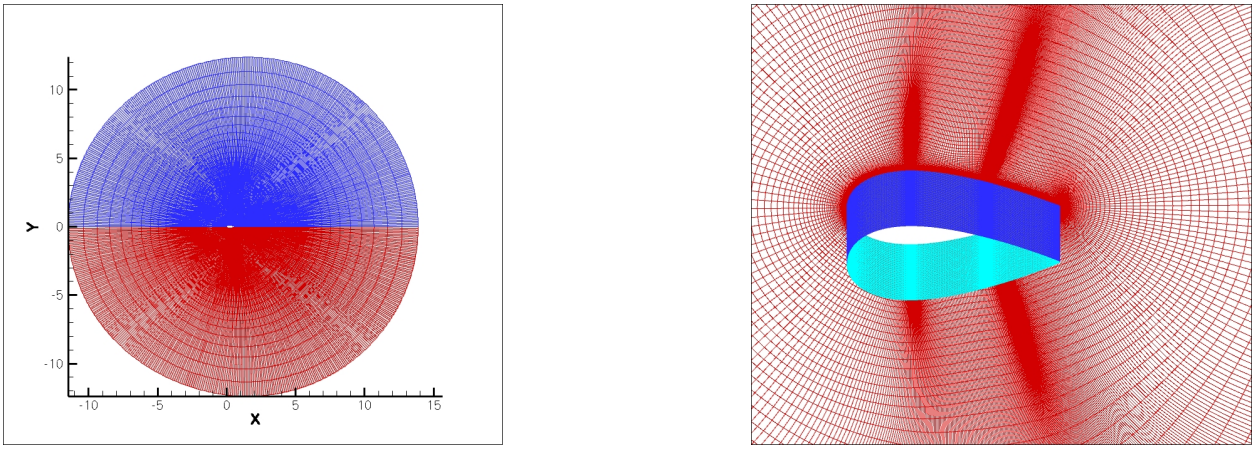

(a) O-type mesh around NACA0036

(b) Three-dimensional mesh for DES

Figure 4. Grid topology for NACA0036 airfoil

Aerodynamic force coefficients C_l and C_d computed from RANS simulation and DES at three angles of attack ($0°, 5°$, and 10^o) are compared in Figure 5. SA-DES is simulated using both two- and three-dimensional mesh topologies, although two-dimensional simulation is not sufficient to predict the inherent nature of the three-dimensional turbulent eddies. It should be noted that C_l becomes negative even at the moderate angle of attack, $\alpha = 5^o$.

No turbulence model in RANS computations appear to reproduce this observation, but SA- and SST-DES simulation can predict this tendency comparatively well. This negative lift coefficient indicates that massive separation can occur for a thick airfoil at low angles of attack. SST-DES is not able to predicate the results as accurately as SA-DES, but it still shows more accurate results than other turbulence models in RANS simulation. Although two-dimensional SA-DES is lacking in reality, the simulation shows good agreement with three-dimensional computations and experiments.

A comparison of the surface pressure distribution at $\alpha = 5^o$ is presented in Figure 6(b), and shows good agreement with experimental data. The eddy viscosity ratio is displayed in Figure 6(a) and shows the

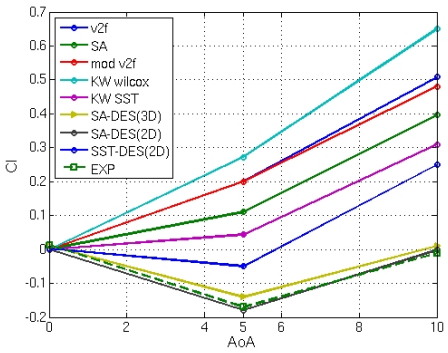

(a) Comparison ofC_l

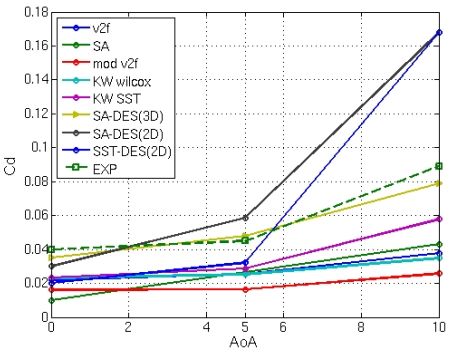

(b) Comparison ofC_d

Figure 5. Comparison of aerodynamic forces using various turbulence modeling

unsteadiness of small vortex shedding. It is evident that the dissipative nature of eddy viscosity is simulated correctly as the distance to the wall increases away from the solid boundaries.

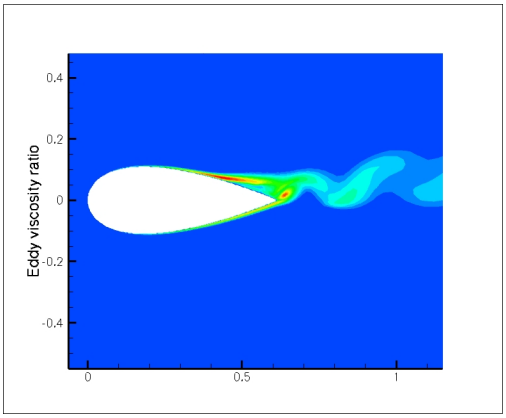

(a) Eddy viscosity ratio ν_t/ν

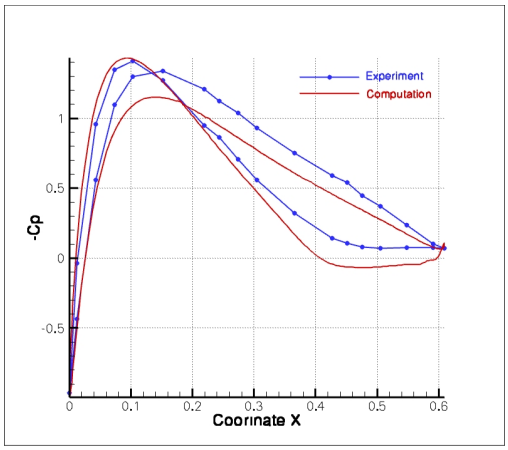

(b) Comparison of Cp

Figure 6. Eddy viscosity ratio and surface pressure at $AOA = 5^o$.

From this validation work it can be inferred that DES results are in general more accurate than RANS simulations, however this accuracy comes at the cost of an increase in computation time. An appropriate mesh resolution within the boundary layer and the near-field should be pre-determined to improve the accuracy of DES computation.

C. Validation III: Flight Test Cases of UH-60A

The last validation is the simulation of UH-60A flights and is more meaningful in that flow field around the complete rotor is analyzed. To reduce the corresponding computational cost, an efficient TS method is applied to simulate three flight test cases. The cost savings and the accuracy of TS method is compared with time-accurate computation for each test case.

D. Three Flight Test Cases

Three steady level flight conditions of UH-60A, flight 8534, 8515, and 9017, are selected for our computation, as they are in the different regimes of the vibration frequencies and the speeds and thus provide the opportunity to investigate the range of the application of time spectral method. Table 1 shows the operating conditions for these cases, and thrust and advance ratio are plotted in Figure 7.[35] It can be expected that

flight 9017 and flight 8515 are rather difficult to predict as accurately as flight 8534, since they are in the dynamic stall regime and in the low speed regime respectively.

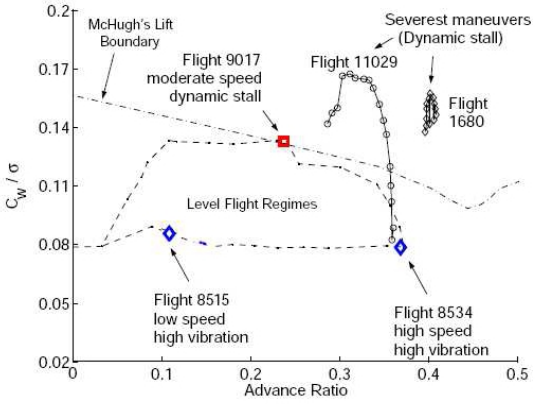

Figure 7. Thrust and advance ratio of UH-60A flight tests.[35]

flight case	8534	8515	9017
omega (rad/sec)	27.025	27.007	26.7821
M_{tip}	0.6415	0.6473	0.6658
M_∞	0.2359	0.0712	0.1578
Advance ratio	0.368	0.11	0.237
Reynolds number	3.22×10^6	9.676×10^6	2.056×10^6
Shaft angle (°)	-7.31	-1.26	-0.15

Table 1. Flight conditions of three steady level flight of UH-60A

A set of single- and multi-block structured meshes were generated with the aid of University of Maryland as part of the DARPA-HQP program and are presented at Figure 8. The single-block mesh in Figure 8(a) contains one blade with a total of 568,816 nodes, while the one shown at Figure 8(b) includes a complete rotor with four blades. The coarse mesh for the rotor consists of 536 multi-blocks with a total of 2,401,776 nodes. A finer mesh with about 17 million nodes is also available and can be used if necessary.

Since the motion of the rotating rotor is highly aeroelastic in nature owing to the strong structural coupling. To make our simulations more realistic, deformation data obtained from the previous coupled CFD/CSD analysis are prescribed at each time step/instance, and the changes of the blade shapes are updated correspondingly as the computation proceeds in time. Deformation data were available from OVERFLOW/CAMRAD simulations performed by Aero Flight Dynamics Directorate (AFDD) at Ames Research Center.[39]

As an alternative to a full rotor simulation, a flow analysis involving only single blade coupled with an appropriate wake geometry has been considered. Although the accuracy of this simulation relies significantly on the types of wake models and the level of blade/wake interferences in the flight state, a saving of the computational cost is great compared to the multi-blade analysis. This approach has shown great success in a number of flight test simulations[40] where wake effects are not dominant. As the wake interference in flight 8534 case has known to be moderate, this technique was applied to flight 8534 simulation, and compared with experimental data. With huge savings in a computational expense and the satisfactory accuracy, an approach using single blade was also employed for parameteric study in the following Section E of the scaling factors of cost savings in TS method.

A second order BDF scheme was used for the time-accurate computation, and a second order upwind scheme with Roe's flux differencing for the inviscid fluxes. Spalart-Allmaras turbulence model was used for the computation of the viscous flux and the turbulence. An efficient multigrid technique was employed to improve the convergence of both time-accurate and time-spectral computations. A total of 15 time instances

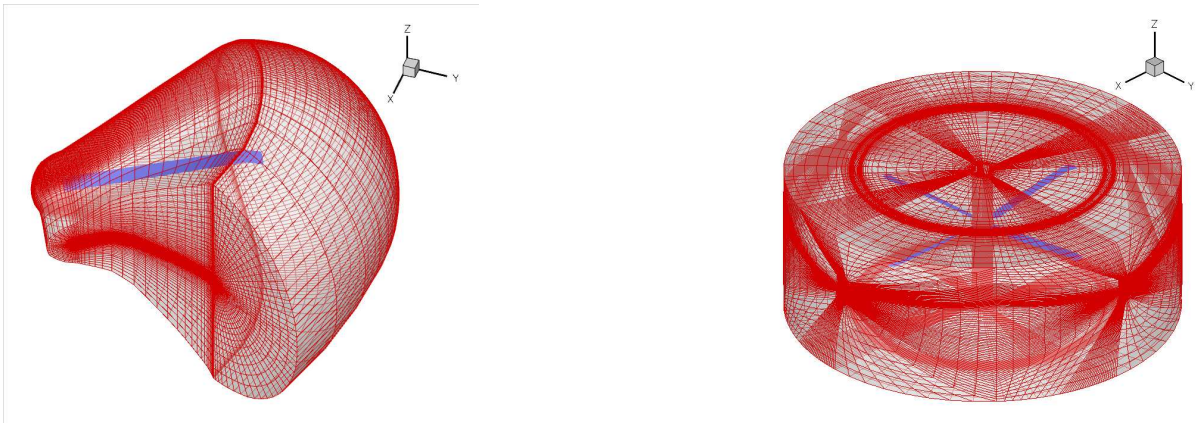

(a) C-O-type mesh around single blade

(b) mesh around 4 blade

Figure 8. Grid topology for UH-60A

were used for the time spectral computations for all test cases, and the results are compared with the time-accurate solutions and experimental data. Both computations were performed at IBM cluster P4+ system at NAVOOCEANO MSRC (Naval Oceanographic Office Major Shared Resource Center). A total of 368 noes were available with each node consisting of eight processors and a memory up to 2 GB was available.

E. Computation Time in Time-Spectral vs. Time-Accurate Method

The problem of how much efficiency we can achieve in computational time without deteriorating the accuracy is substantial, when we use TS method. A direct comparison of wall clock CPU time for both computation methods can be a reasonable way to estimate the efficiency of TS method. A flight 8534 test case was simulated for this study, and a single blade analysis coupled with the free wake geometry was performed. Although the results from four blade simulations which will be shown later demonstrate better accuracy, a single blade analysis was sufficiently accurate to perform this study.

A total of 16 processors in SGI Origin 2000 machine (with up to 16GB memory) were used for both computations, and a total of 15 time instances are employed for TS computation. As the memory requirements of TS method is larger to store the meshes and the solution files at all time levels, a machine with shared memory was preferred. A wall clock CPU time per one full multigrid cycle (3W) for each method is shown at Table 2. For both computational methods to achieve the convergence of the same order of magnitude, l_2 norm based residual of density is compared. A total of $1,000 \sim 1,500$ multigrid cycles for TS computation are required for the desirable convergence (10^{-4}) and about $2.5 \sim 3$ revolutions for time-accurate computations. The convergence history of the density residual for TS simulation is plotted at Figure 9.

A CPU time for the whole simulation can be estimated based on the values in Table 2. It was observed during our study that a time-accurate computation converges after about three revolutions with 0.2° time step, and it requires about 30 multigrid cycles for the inner iterations by the dual-time stepping technique. Thus the total CPU time required is $724,140sec$ ($360^\circ / \ 0.2^\circ \times 3 \ rev \times 30 \ MGcycle \times 4.47sec$) On the other hand, TS simulation converges after about $1,500$ multigrid cycles, and a total of $138,000sec$ ($1,500 \ MGcycle \times 92sec$) is necessary. We can infer that the employment of TS method leads to the cost savings more than five times of time accurate computation. Although computation time for preprocessing for mesh partitioning is longer in TS computation, a total amount of time saving is still considerable.

The scaling factor of the cost savings with respect to the number of time instances is also important to

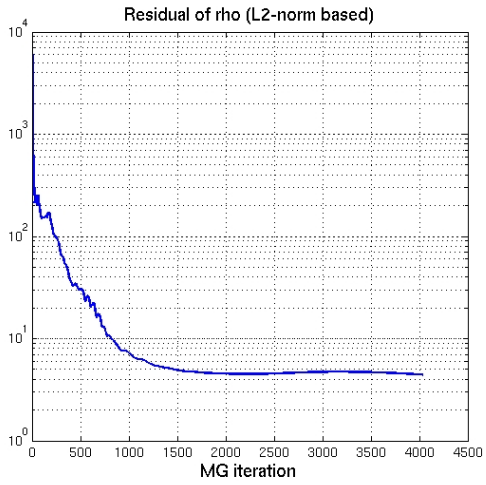

Figure 9. Convergence history of time-spectral computation

scheme	computation time (sec)
TA	4.47
TS	92

Table 2. computational costs per one MG cycle

accomplish the overall efficiency of TS method. A wall clock CPU times for one multigrid cycle corresponding to 3,5,9,15 and 25 time instances are plotted Figure 10 and compared with linear scalability. The scaling factor of TS method is not exactly linear, and this is due to the time derivative term in Equation 9 which involves the multiplication of matrix and vector.

F. The Number of Time Instances in Time-Spectral Method

The problem of how many time instances are necessary to achieve the same level of accuracy of the time-accurate computation is very critical to maximize its efficiency. It will be ideal to use the least number of time instances which can achieve the equivalent accuracy. This problem is closely related to the Nyquist-Shannon sampling theorem,[38] and it implies that the exact reconstruction of the time-accurate solutions is possible if the frequency contents of the solutions are band-limited and the sampling frequency is greater than twice the bandwidth (*Nyquist frequency*). A close investigation on the frequency contents of the time-accurate solutions should be preceded before we discuss the accuracy of TS method. Figure 11, 12 and 13 show the frequency contents of the sectional normal forces computed by the time-accurate method corresponding to the flight 8534, 8515, and 9017 cases respectively. The four blade analysis was employed for all computations. It is observed from the plots that the signals are band-limited within certain frequency content. However, the total number of frequency contents below Nyquist frequency is not trivial, and if we want to employ all of them, we can not guarantee the efficiency of the TS computation in our study. Thus a problem still remains about how much accuracy we can achieve with less number of time instances than required by Nyquist frequency. Another issue of significance is that of the aliasing errors for TS computation. Thus the experiment of changing the number of time instances ranging from three to fifteen is conducted, and the results are shown at Figure 14, 15, and 16 and compared with the time-accurate solutions. The sectional normal forces of flight 8534 were computed using four blade analysis, and the excellent agreements with the time-accurate computation are observed as the number of time instances increase. It can be inferred from the plots that the results appear to have converged with nine or more time instances, since not much improvement in accuracy is noticeable beyond those time instances. This fact also indicates that the first few frequencies will be sufficient to reconstruct the time-accurate solutions without the concern of the aliasing errors, as those have the dominant effects on the entire frequency spectrum and the amplitudes of the rest of the frequencies are relatively much smaller. Although the simulations in Section G employed fifteen time

instances for all flight test cases to minimize the possibility of the aliasing errors, it should be noted that the smaller number of time instances will greatly enhance the efficiency of TS method while satisfying the accuracy, and thus the saving factor of five or more in Section E can be even larger.

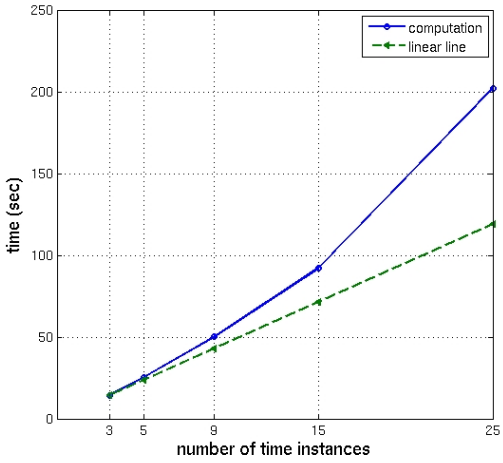

Figure 10. Computation time with respect to the number of time instances (solid line - computation)

G. Simulation Results

The simulation of three flight tests are performed by both single- and multi-blade analysis. Sectional normal forces, chord forces, and pitching moments are computed for each flight test using time-accurate and time-spectral method, and the values at nine locations along the span are compared with the experimental data.[36,37]

First the analysis of the flight 8534 simulation is performed using a single blade with wake coupling and the results are shown in Figure 17, 18, and 19. A wake geometry is updated at every revolution based on the solutions calculated at the previous revolution. As mentioned earlier, the accuracy of single-blade analysis with wake coupling is considerably dependent on the nature of the flight state, i.e. how much interaction takes place between the blades and the wakes. As flight 8534 case shows very little interaction, the agreements with the experiments are excellent. The great agreement between time-accurate and time-spectral method should be noted as well. The simulations of flight 8515 and 9017 have been carried out too, but the corresponding results do not show as good agreement as in flight 8534 case. Thus only the results of flight 8534 simulation was included in this paper.

Subsequently the analyses using a complete rotor are conducted for all flight test cases, and shown at the following Figures. Both the coarse mesh ($\sim$ 2.4 million) and the fine mesh ($\sim$ 17million) are available, and the simulations for all test flight cases have been duplicated with the fine mesh in the study not shown in this paper, however the improvement in the accuracy has not shown to be very remarkable for flight 8534 and 9017 case, and thus only the results of flight 8515 simulation is updated with a finer mesh. It is likely that the resolution of the coarse mesh have converged without the need of further refinement. Figure 20, 21, and 22 show the results from the simulation of flight 8534. The results from flight 8515 simulation are plotted at Figure 23, 24, and 25, and flight 9017 simulation at Figure 26, 27, and 28. The differences in the results between time-accurate and time-spectral computations are very little for all flight test simulations, and match very well. It can be certainly expected that the results from the rotor analysis is more accurate than the single blade analysis, and the most distinctive improvement is seen in the pitching moment at Figure 19 and 22. Excellent agreements are demonstrated in the flight 8534 simulation. As the flight 8515 and flight 9017 are more difficult to predict because of their flight characteristics (low speed transition, dynamic stall), the accuracy of the time-accurate computations is not as good as in flight 8534 case and yet a good agreement between computation and the experiments is observed for both flight test cases. The interaction with the bundled disc vortices causes the impulsive loading in flight 8515. The analysis shows good qualtitative correlation and fair quantitiative correlation in resolving this phenonmenon. The flight

9017 case experiences two stalls on the retreating side, $200^\circ \sim 360^\circ$, making accurate simulation more challenging. While the prediction of time-accurate method seem resolve the stall phenomena relatively well, time-spectral method is lacking in the accuracy on the stall prediction in flight 9017 test case. The accuracy can be improved by employing more number of time instances in TS simulations.

IV. Conclusions and Future Work

Accuracy and the efficiency of our aerodynamic analysis tools were examined by simulating the flow conditions commonly encountered in a helicopter flight; two-dimensional dynamic stall around pitching airfoils (NACA0015 & SC1095 airfoils), massive separation around bluff body (represented by NACA0036 airfoil), and the full flight tests (8534, 8515, and 9017) of UH-60A configuration. RANS simulation with various turbulence models was used for all validation cases. The capability of each turbulence model to predict the turbulent properties of dynamic stall phenomena was examined, and results are compared with experiments. It is not straightforward to find a particular turbulence model which shows the best accuracy for all cases, which signifies the difficulty of RANS approximation to simulate highly turbulent flows. DES, which is a hybrid technique that combines the favorable aspects of RANS and LES, was employed for the prediction of the massive separation around NACA0036 airfoil. The DES simulation shows great improvement in predicting the properties of highly turbulent flows compared to the RANS computation. Time-spectral method was selected as an efficient algorithm and applied to the simulation of three test cases of UH-60A flight. A significant reduction in the computational cost stems from its Fourier series form of the periodic time response and the assumption of periodic steady-state. Good agreement between time-accurate and time-spectral method is noted for all the flight test cases. Also, predictions from both methodologies match quite well with the experimental data. Because of its steady state formulation, the TS method allows easier incorporation of the adjoint based formulation for design optimization. Thus the TS method shows great potential for application to helicopter design problems in the future.

V. Acknowledgment

This work has been carried out under the support of the AFDD at Ames Research Center, under contract NNA06CB11G. We gratefully acknowledge the support of our point of contact, Mark Potsdam, Chee Tung and Tom Maier, in supplying us with the meshes and experimental data necessary to complete this study.

References

[1]J. Sitaraman, A. Datta, J. Baeder, and I. Chorpa, "Coupled CFD/CSD Prediction for Rotor Aerodynamic and Structural Dynamic Loads for Three Critical Flight Conditions," *31st European Rotorcraft Forum*,Firenze, Italy, 2005.

[2]P. B. Martin, C. Tung, M.S. Chandrasekhara, and E. Arad. "Active Separation Control: measurements and Computations for a NACA0036 Airfoil," *AIAA-2003-3516*, 2003.

[3]E. Arad, P. B. Martin, J. Wilson, and C. Tung, "Control of Massive Separation on A Thick-Airfoil Wing: A Computational and Experimental Study," *44th AIAA Aerospace Sciences Meeting and Exhibit*, Reno, Nevada, Jan. 9-12, 2006.

[4]K. D. Squires, "Detached-Eddy Simulation: Current Status and Perspectives," *Proceedings of Direct and Large-Eddy Simulation-5*, 2004.

[5]J. S. Wilson "Turbulence Measurements on a 2D NACA0036 with Synthetic Jet Flow Control," *62nd Annual Forum of the American Helicopter Society*, Phoenix, Arizona, May 9–11, 2006.

[6]E. van der Weide, G. Kalitzin, G. Schluter, J. J. Alonso,, "Unsteady Turbomachinery Computations Using Massively Parallel Platforms," *AIAA Paper 2006-0421*, Reno, NV, January 2006.

[7]P. R. Spalart, and S. R. Allmaras, "A One-Equation Turublence Model for Aerodynamic Flows," *AIAA Paper 92-0439*, 1992.

[8]P. R. Spalart, and S. R. Allmaras, "A One-Equation Turublence Model for Aerodynamic Flows," *La Recherche Aerospatiale n1, 5-21*, 1994

[9]D. C. Wilcox, "Turbulence Modeling for CFD," *DCW Industries*, Dec., 2002.

[10]F. R. Menter, "Two-equation eddy-viscosity turbulence models for engineering applications," *AIAA Journal, vol. 32, pp. 269-289*, 1994

[11]G. Kalitzin, G. Medic, G. Iaccarino, and P. Durbin, "Near-wall behavior of RANS turbulence models and implications for wall functions," *Journal of Computational Physics, vol. 204, pp. 265-291*, 2005

[12]P. Durbin, "Separated flow computations with the $k-\epsilon-v^2$ model," *AIAA Journal, vol. 33, pp. 659-664*, 1995.

[13]P. Durbin, "Near wall turbulence closure modleing without damping functions," *Theo. Comp. Fluid Dyna. vol.3*, 1991.

[14]G. Kalitzin, G. Medic, G. Iaccarino and P. Durbin "Near-wall behavior of RANS turbulence models and implications for wall functions," *Journal of Computational Physics, Volume 204, Issue 1, pp. 265-291*, March 2005.

[15]K. Duraisamy, and G. Iaccarino, "Curvature correction and application of the $v^2 - f$ turbulence model to tip vortex flows," *Center for Turbulence Research Annual Research Briefs*, 2005.

[16]K. Duraisamy , W. J. McCroskey, J. D. Baeder, "Analysis of Wind Tunnel Wall Interference Effects on Unsteady Subsonic Airfoil Flows," *AIAA-2006-2993*, Reno, NV, Jan. 2006.

[17]B. A. P. Reif, P. Durbin, A. Ooi, "Modeling rotational effects using eddy-viscosity closures," *International Journal of Heat Fluid Flow, vol.20, pp. 563-573*, 1999.

[18]J. S. Chow, G. Zilliac, and P. Bradshaw, "Mean and turbulence measurements in the near field of a wingtip vortex," *AIAA Journal. vol. 35, pp. 1561-1567*, 1997

[19]J. S. Baggett, J. Jimenez, and A. G. Kravchenko, "Resolution requirements in large-eddy simulations of shear flows," *Annual Research Briefs*, Center for Turbulence Research, NASA Ames/Stanford, 1997

[20]G. Kalitzin, J. A. Templeton, and G. Medic, "A near-wall eddy-viscosity formulation for LES.," *Symposium on Complex Effects in Large Eddy Simulation,*, Limassol, Cyprus, 2005

[21]P. R. Spalart, W. -H. Jou, M. Stretlets, and S. R. Allmaras, "Comments on the Feasibility of LES for Wings and on the Hybrid RANS/LES Approach," *Proceedings of the First AFOSR International Conference on DNS/LES*, 1997

[22]M. Strelets, "Detached Eddy Simulation of Massively Separated Flows," *AIAA 2001-0879*

[23]A. Jameson, "Time dependent calculations using multigrid, with application to unsteady flows past airfoils and wings," *AIAA Journal, 91-1956,* June 1998.

[24]K. C. Hall, J. P. Thomas, and W. S. Clark. "Computation of unsteady nonlinear flows in cascades using a harmonic balance technique," *AIAA Journal, 40(5):879–886,* May 2002.

[25]M. S. McMullen, "The Application of Non-Linear Frequency Domain Methods To the Euler and Navier-Stokes Equations ," *Ph.D thesis, Stanford University,* March 2003.

[26]F. Kachra and S. K. Nadarajah, "Viscous Aeroelastic Solutions Using the Non-Linear Frequency Domain Method," *24th Applied Aerodynamics Conference,* June 5-8, San Francisco, California.

[27]A. K. Gopinath, and A. Jameson. "Time Spectral Method for Periodic Unsteady Computations over Two- and Three-Dimensional Bodies," *AIAA-2005-1220,* Jan. 2005.

[28]A. K. Gopinath, and A. Jameson "Application of the Time Spectral Method to Periodic Unsteady Vortex Shedding," *AIAA-2006-0449,* Jan. 2006.

[29]E. van der Weide, A. Gopinath, and A. Jameson, "Turbomachinery Applications with the Time Spectral Method," *AIAA-2005-4905,* Toronto, Canada, June 2005.

[30]G. Medic, G. Kalitzin, D. You, E. van der Weide, J. J. Alonso, and H. Pitsch, "Integrated RANS/LES Computations of an Entire Gas Turbine Jet Engine," *AIAA Paper 2007-1117,* Reno, NV, January 2007.

[31]C. Canuto, M. Y. Hussaini, A. Quarteroni, T. A., Jr. Zang "Spectral Methods in Fluid Dynamics," *Springer,* 1998.

[32]K.Lee, J.J.Alonso, and E.v.d.Weide, "Mesh Adaptation Criteria for Unsteady Periodic Flows Using a Discrete Adjoint Time-Spectral Formulation," *AIAA-2006-692,* Reno, NV, Jan. 9-12, 2006.

[33]P. R. Spalart, "Young-Person's Guide to Detached-Eddy Simulation Grids," *NASA/CR-2001-211032,* 2001.

[34]A. R. Piziali "An experimental investigation of 2D and 3D oscillating wing aerodynamcis for a range of angles of attack including stall," *NASA TM 4632,* 1994.

[35]A. Datta, and I. Chopra "Prediction of UH-60A Dynamic Stall Loads in High Altitude Level Flight using CFD/CSD Coupling," *61st Annual Forum of the American Helicopter Society,* grapevine, Texas, June1–3, 2005.

[36]Bousman, G. and Kufeld, R.M., Balough, D., Cross, J.L., Studebaker, K.F. and Jennison, C.D. "Flight Testing the UH-60A Airloads Aircraft," *50th Annual Forum of the American Helicopter Society,* Washington, D.C., May 1994.

[37]Kufeld, R. M., and Bousman, W. G. "UH-60A Airloads Program Azimuth Reference Correction," *Technical Note, Journal of the American Helicopter Society,Vol.50, No.2, pp.211-213* 2005.

[38]E. Oran Brigham, "The fast Fourier transform and its applications," *Englewood Cliffs, N.J. : Prentice Hall,* 1998.

[39]M. Potsdam, H. Yeo, and W. Johnson, "Rotor Airloads Prediction Using Loose Aerodynamic/Structural Coupling," *Proceedings of the American Helicopter Society 60th Annual Forum*,Baltimore, MD, June 2004.

[40]A. Datta, J. Sitaraman, I. Chopra, and J. Baeder, "CFD/CSD Prediction of Rotor Vibratory Loads in High-Speed Flight," *Journal of Aircraft, Vol.43, No.6*,2006.

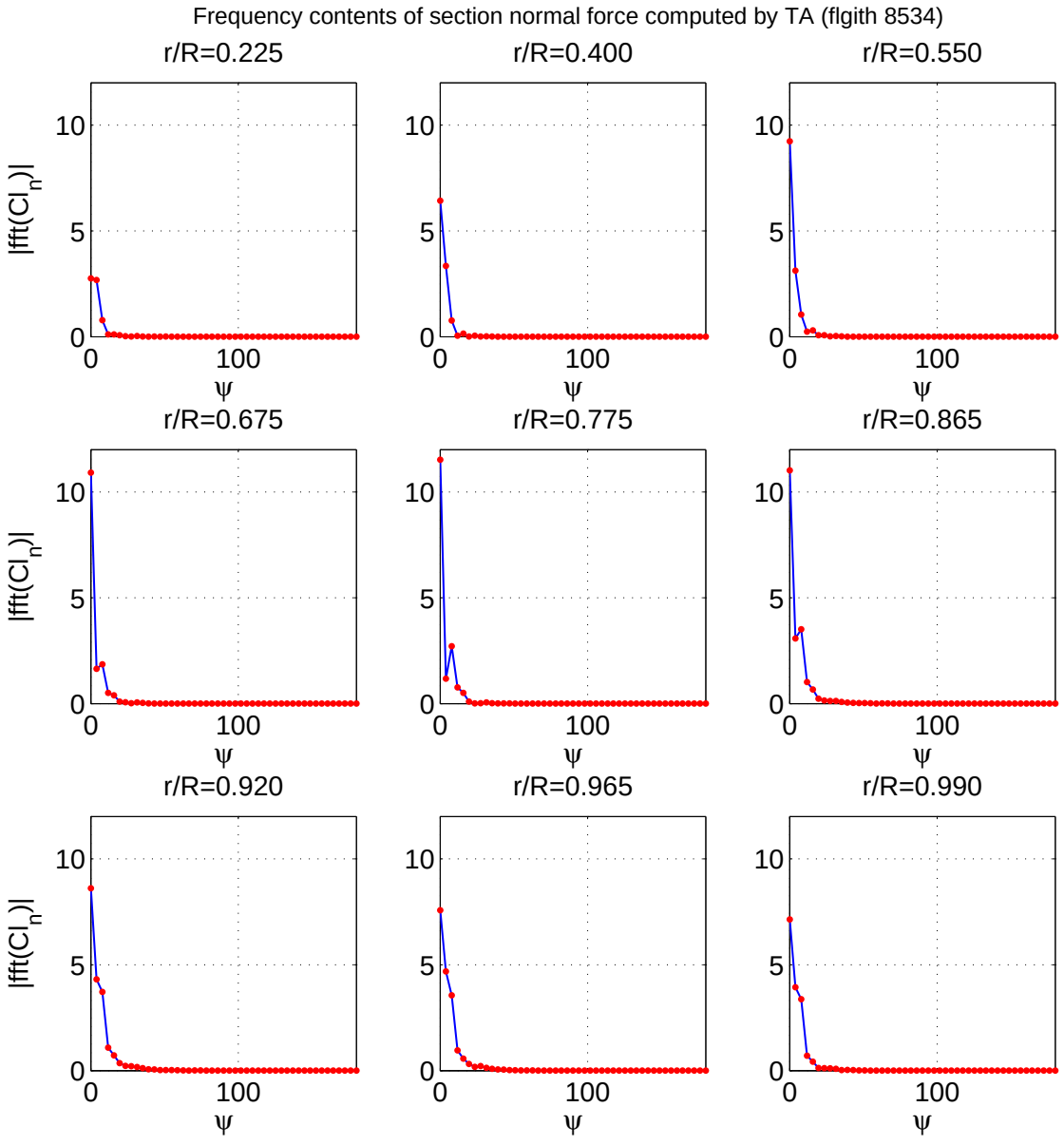

Figure 11. Frequency contents of sectional normal force computed by TA (flight 853 4))

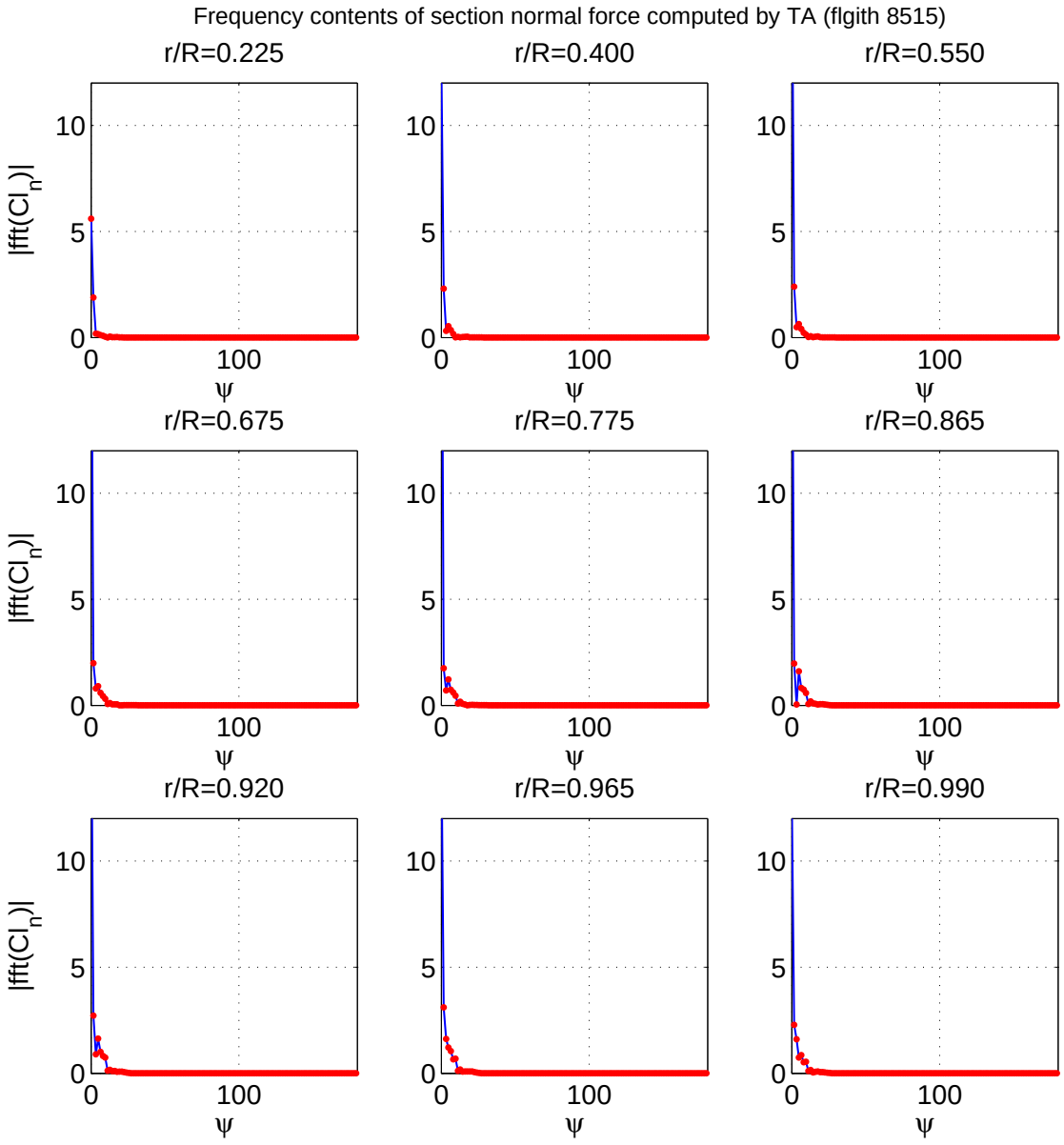

Figure 12. Frequency contents of sectional normal force computed by TA (flight 851 5))

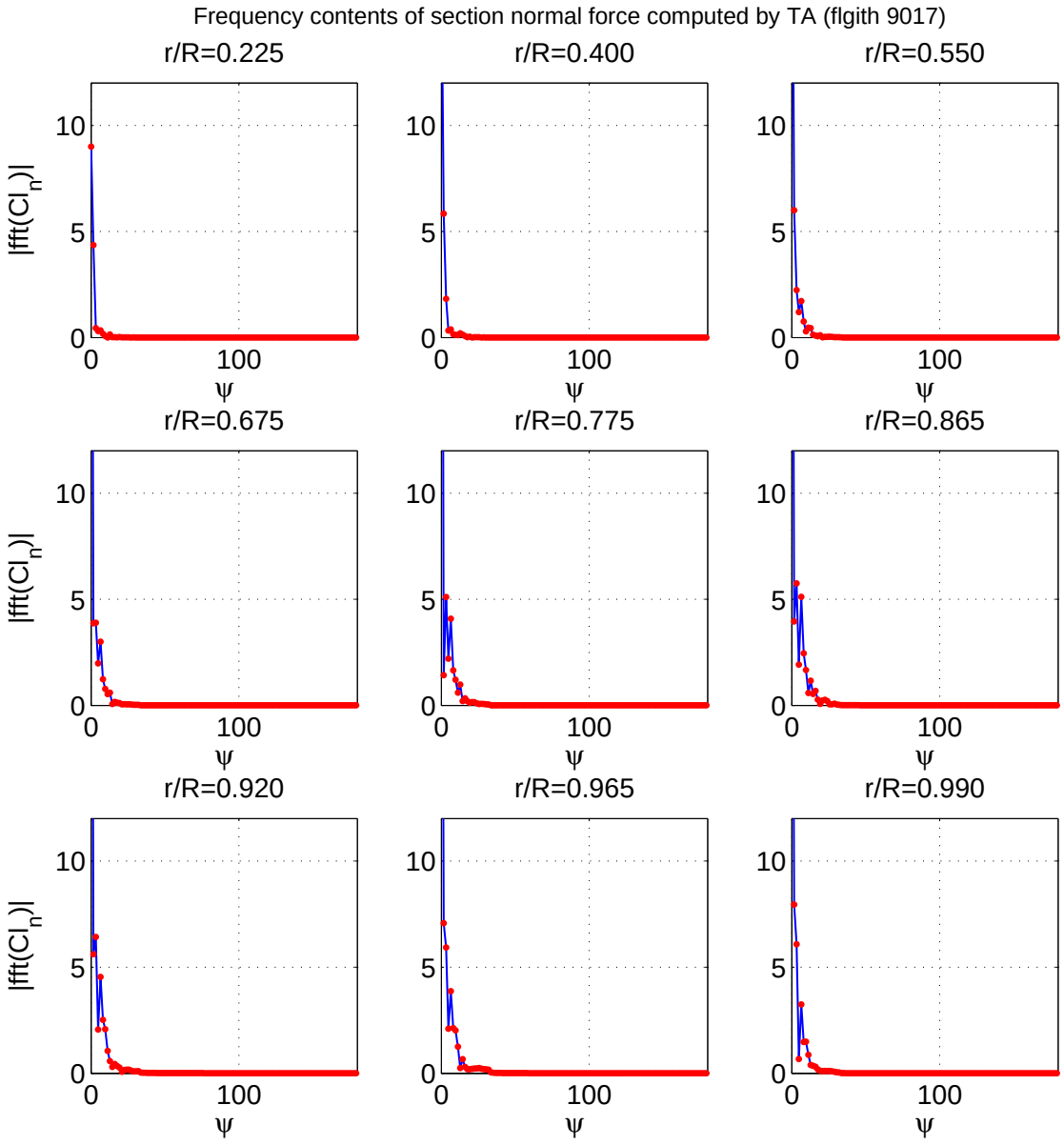

Figure 13. Frequency contents of sectional normal force computed by TA (flight 901 7))

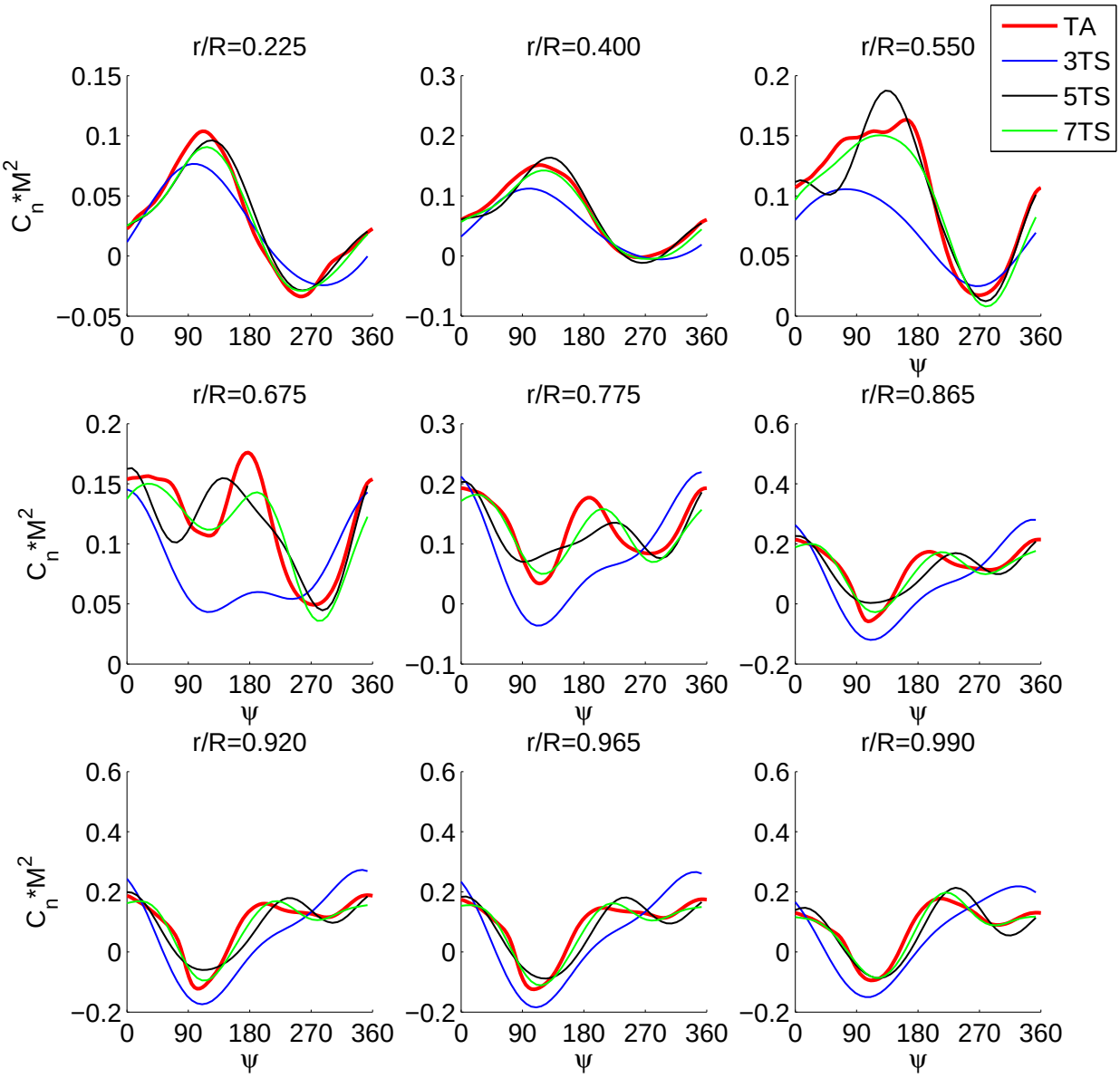

Figure 14. Section normal forces corresponding to the different numbers of time in stances (3, 5, and 7), flight 85345 (using 4 blade mesh)

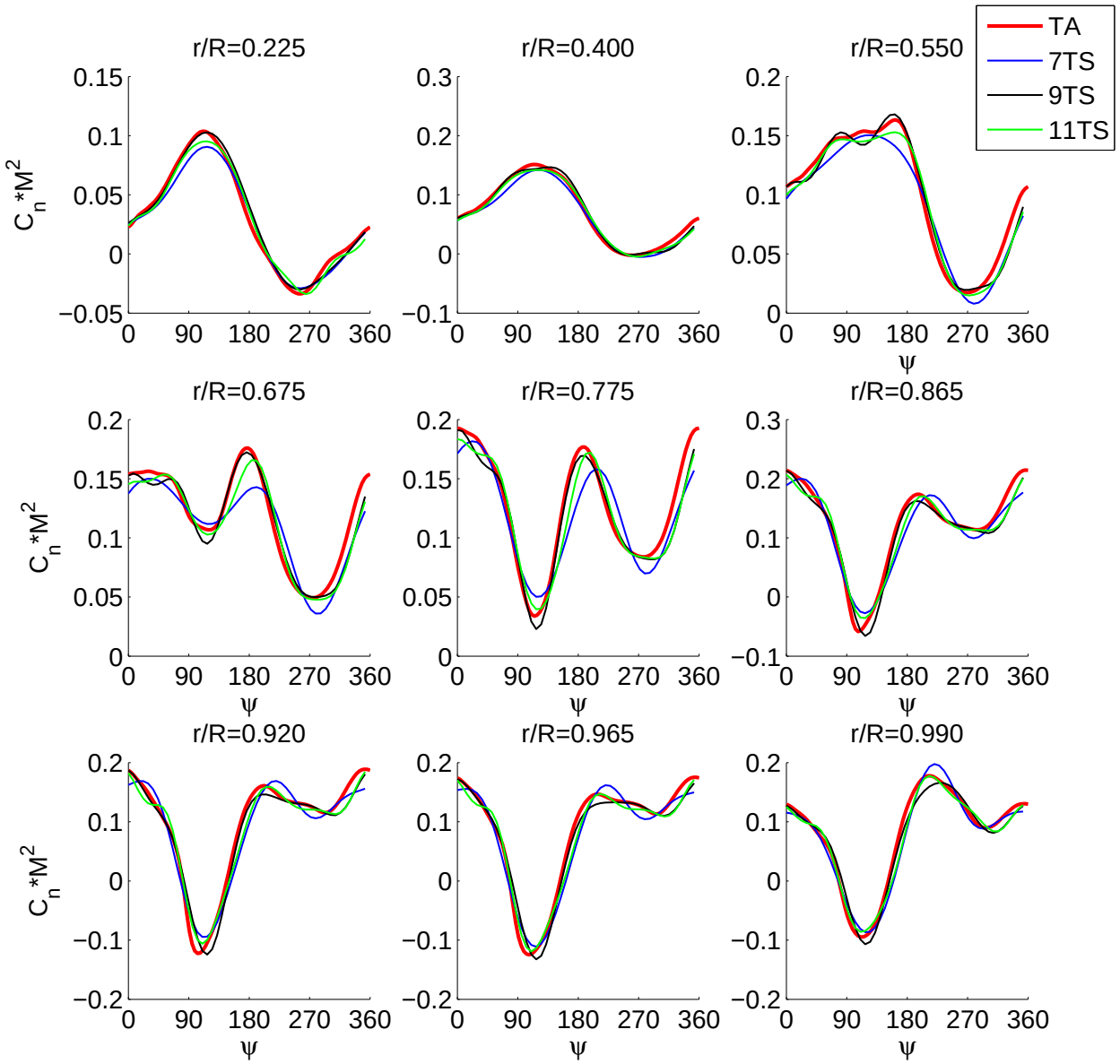

Figure 15. Section normal forces corresponding to the different numbers of time in stances (7, 9, and 11), flight 85345 (using 4 blade mesh)

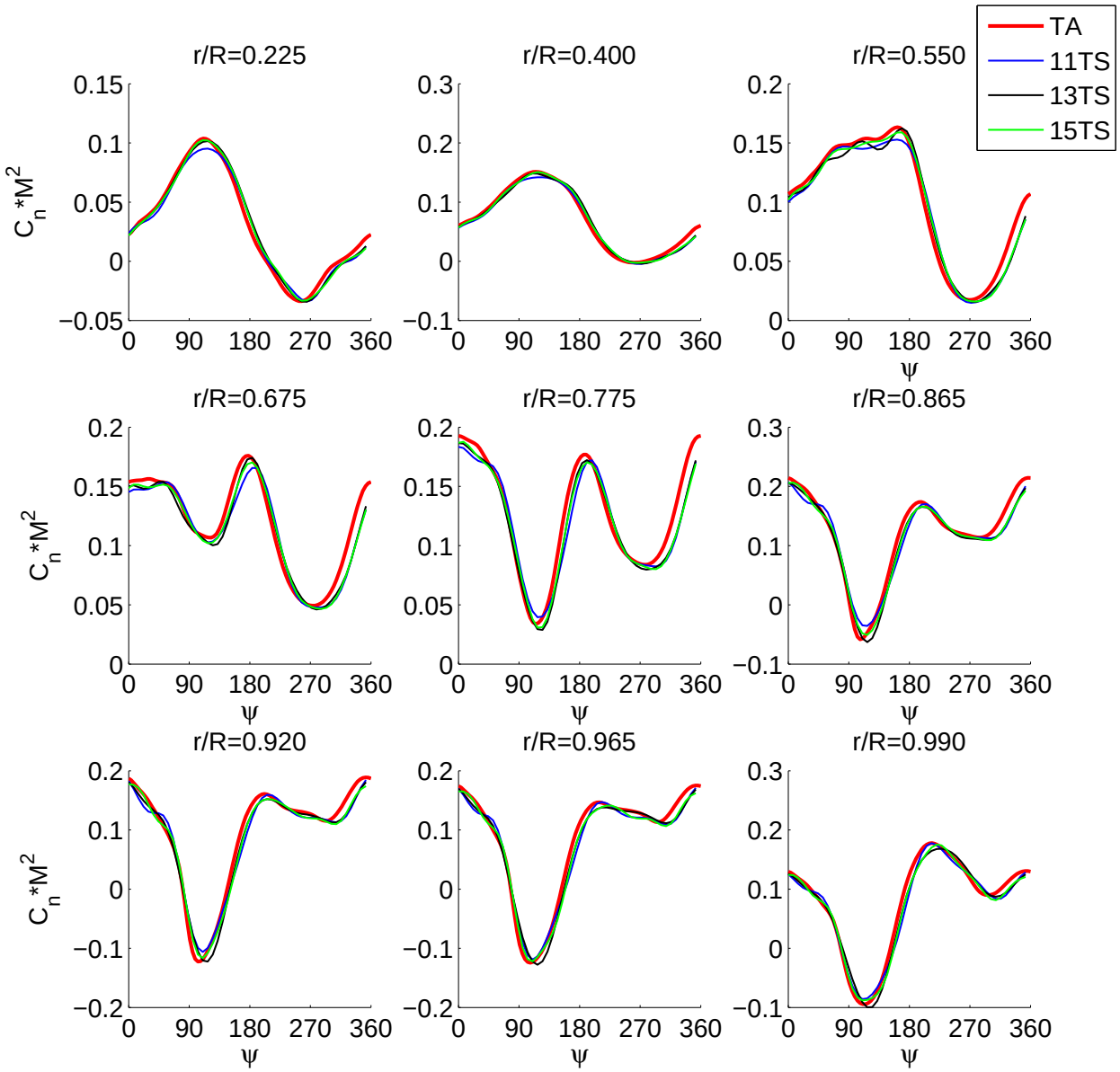

Figure 16. Section normal forces corresponding to the different numbers of time in stances (11, 13, and 15), flight 85345 (using 4 blade mesh)

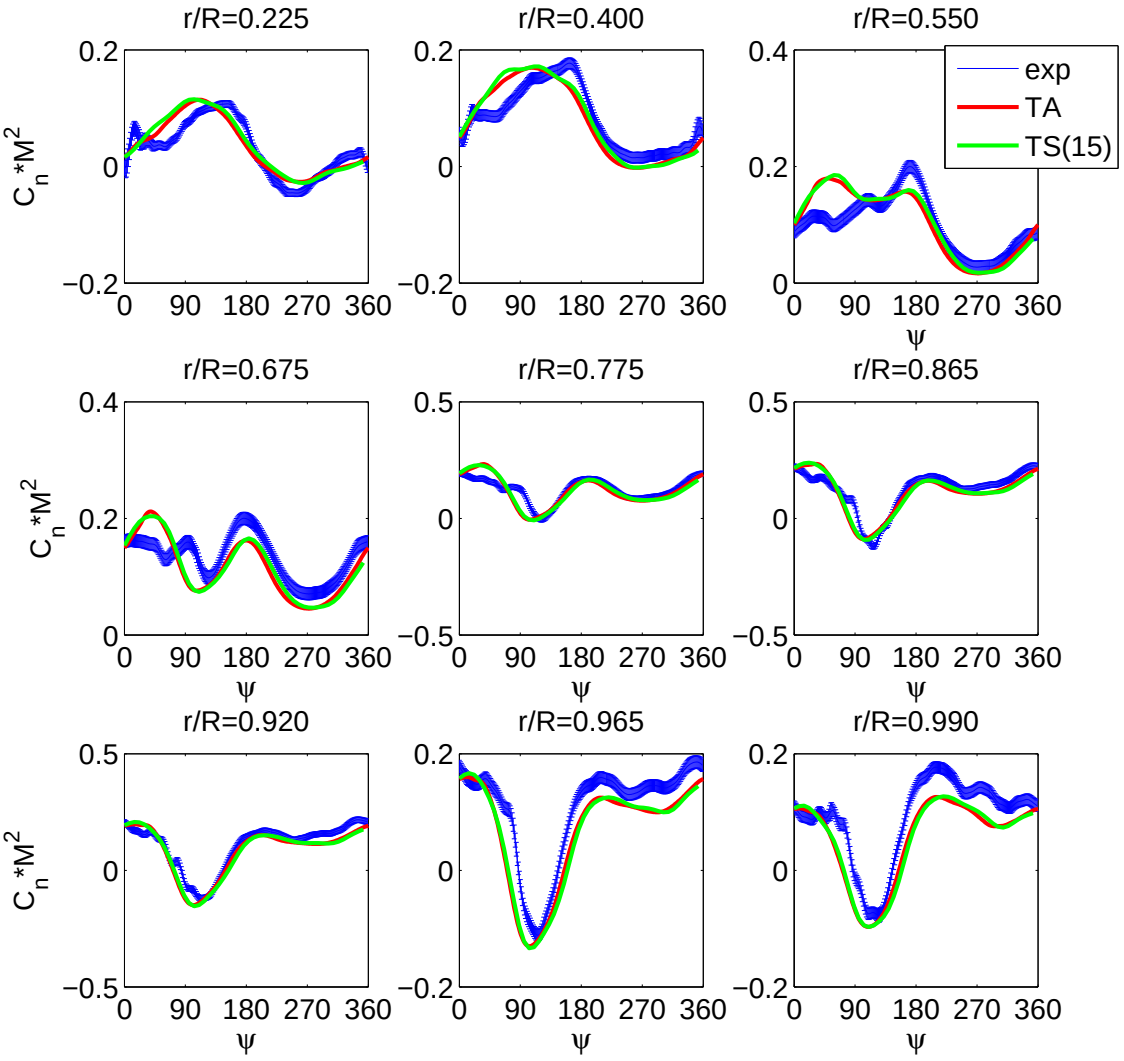

Figure 17. Section normal force of flight 8534 (one blade case with wake coupling (red-TA; green-TS)).

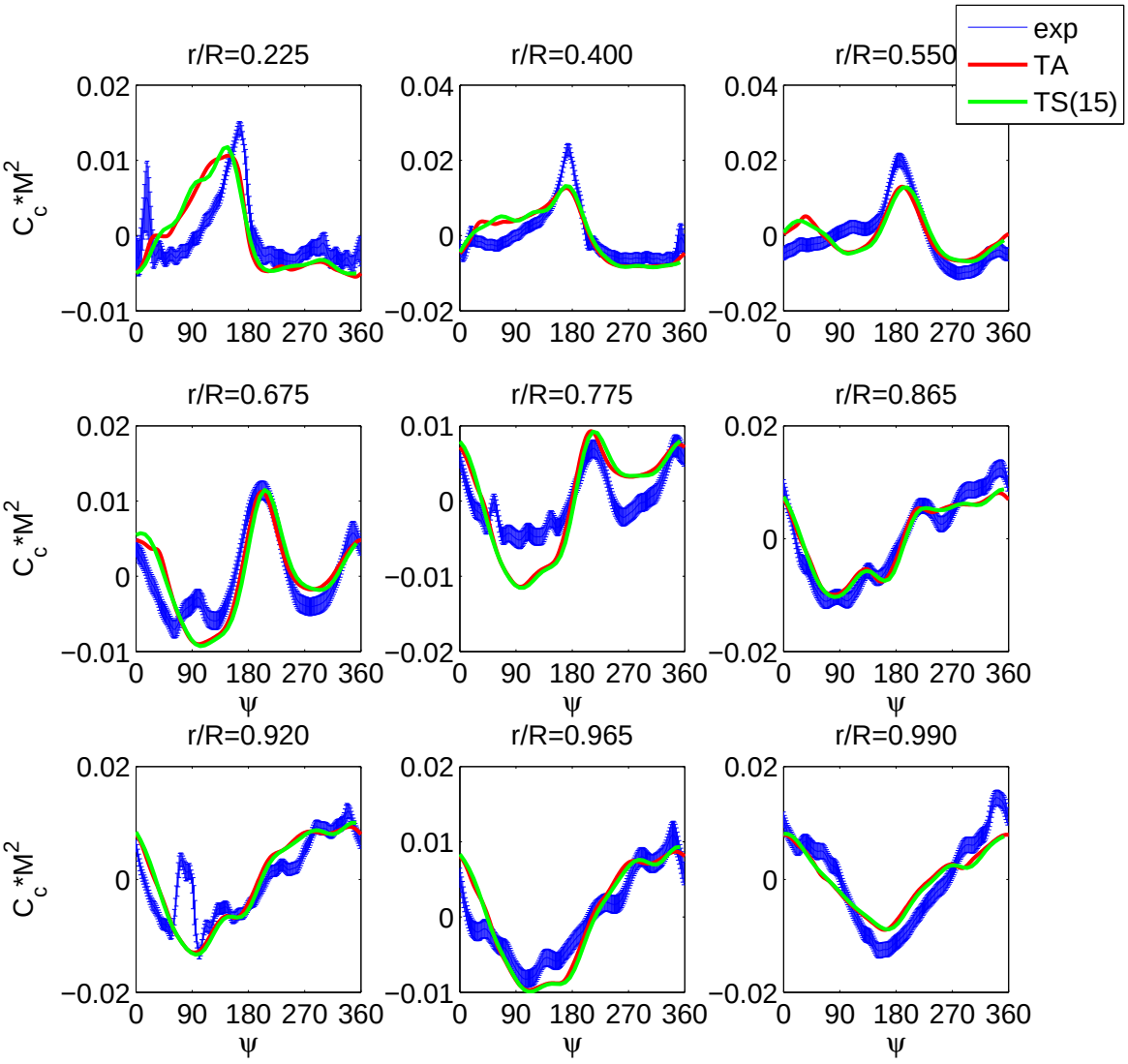

Figure 18. Section chord force of flight 8534 (one blade case with wake coupling (red-TA; green-TS)).

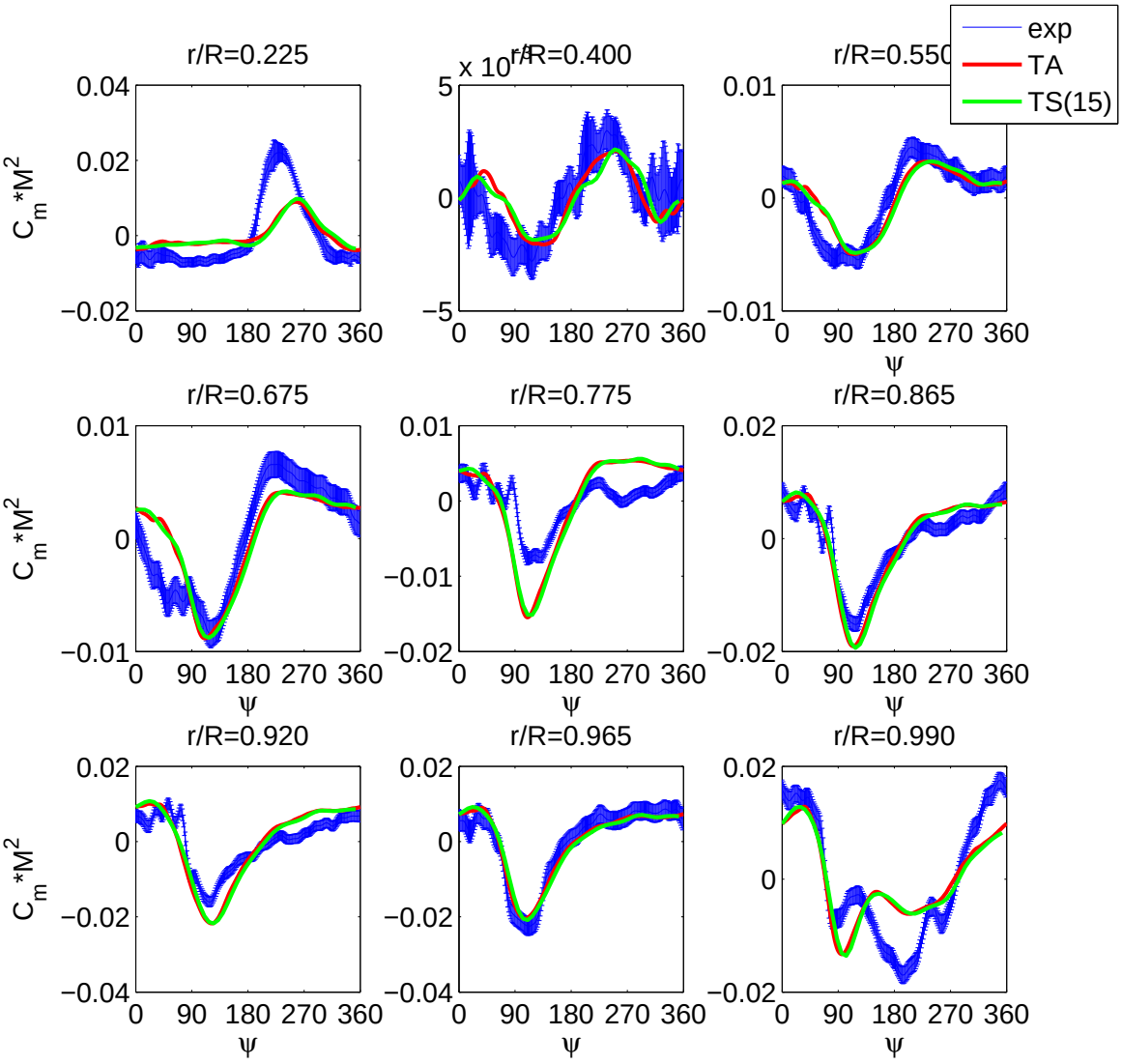

Figure 19. Section pitching moment of flight 8534 (one blade case with wake coupling (red-TA; green-TS)).

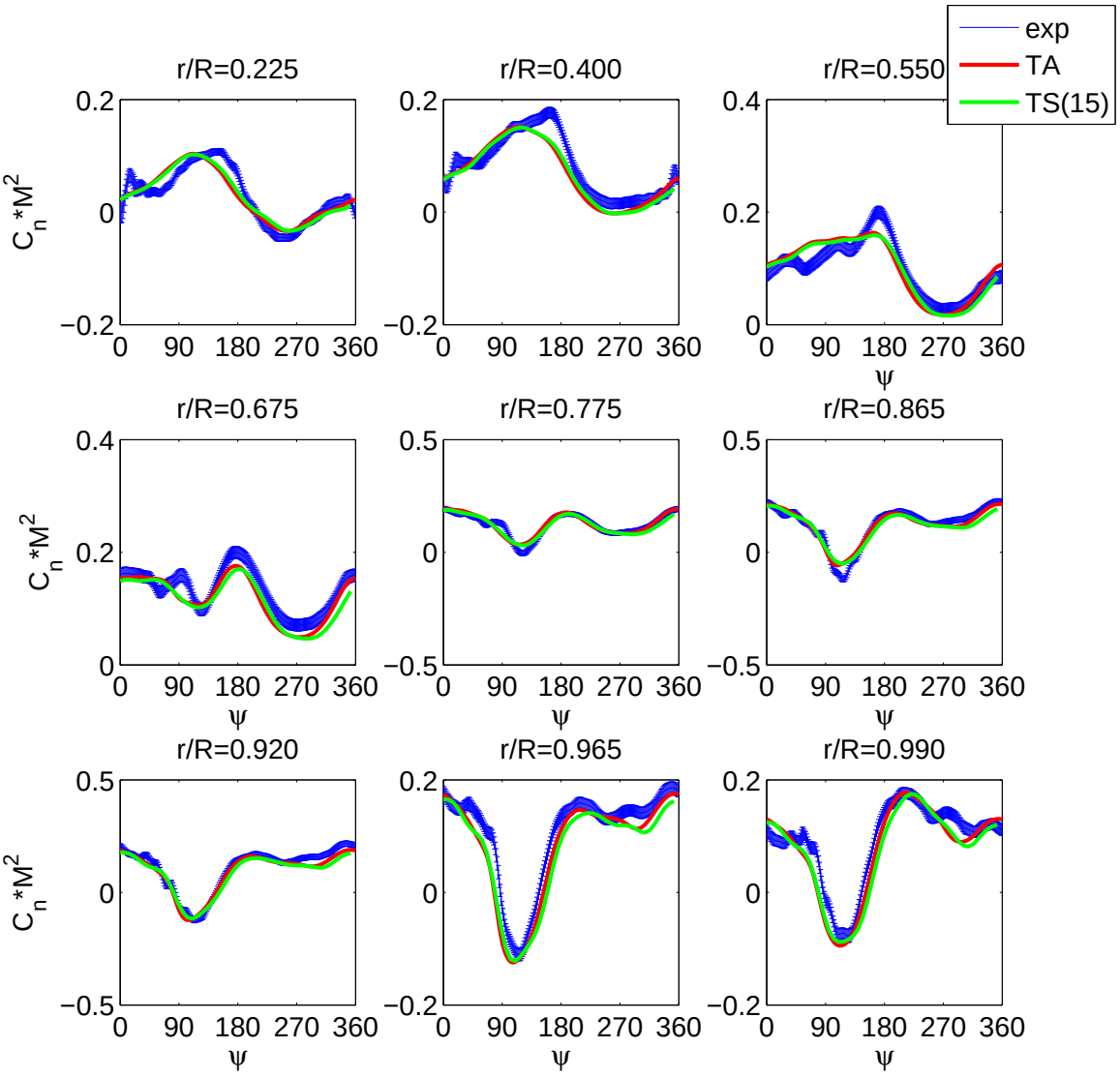

Figure 20. Section normal force of flight 8534 (four blade case (red-TA; green-TS)).

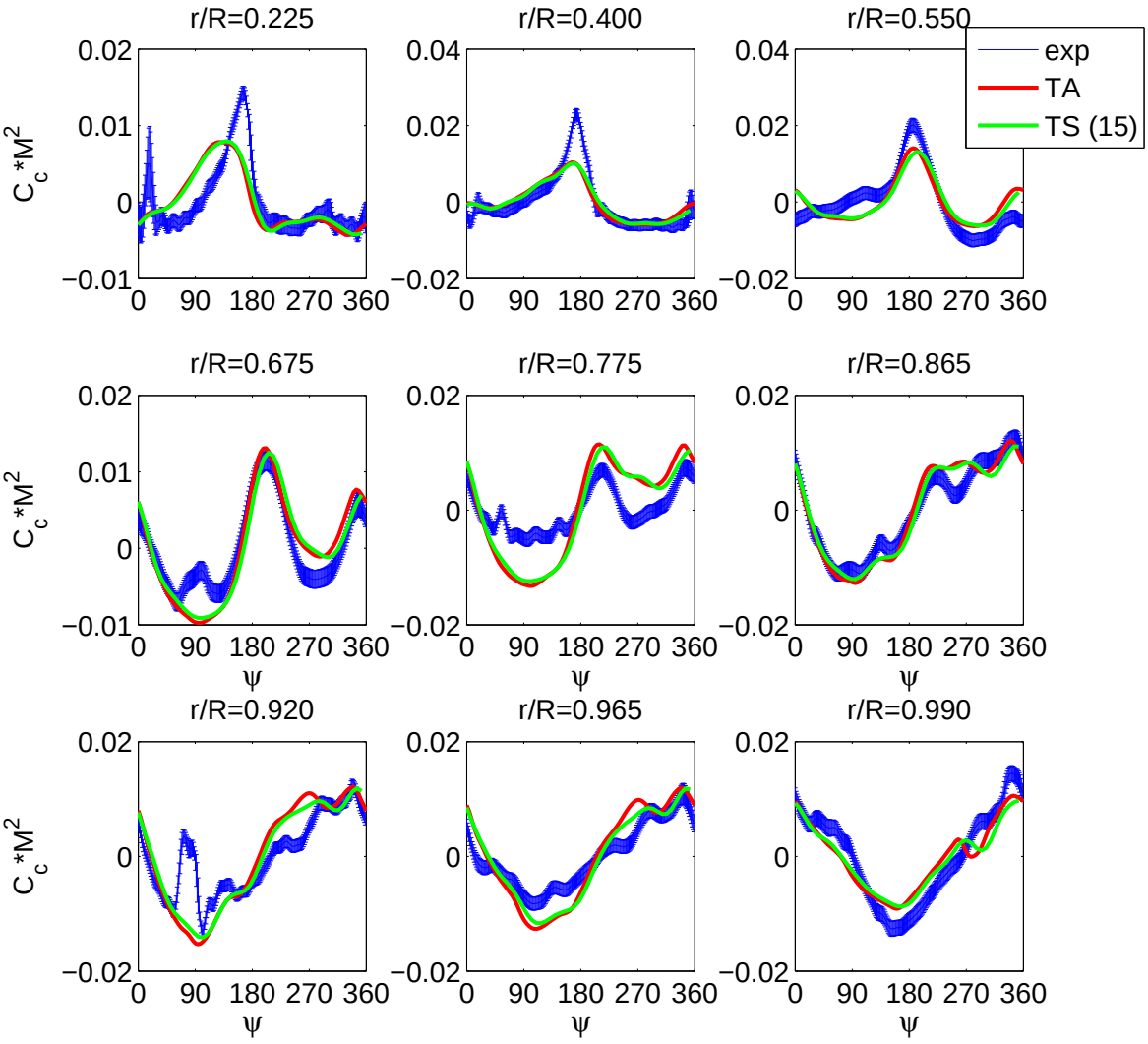

Figure 21. Section chord force of flight 8534 (four blade case (red-TA; green-TS)).

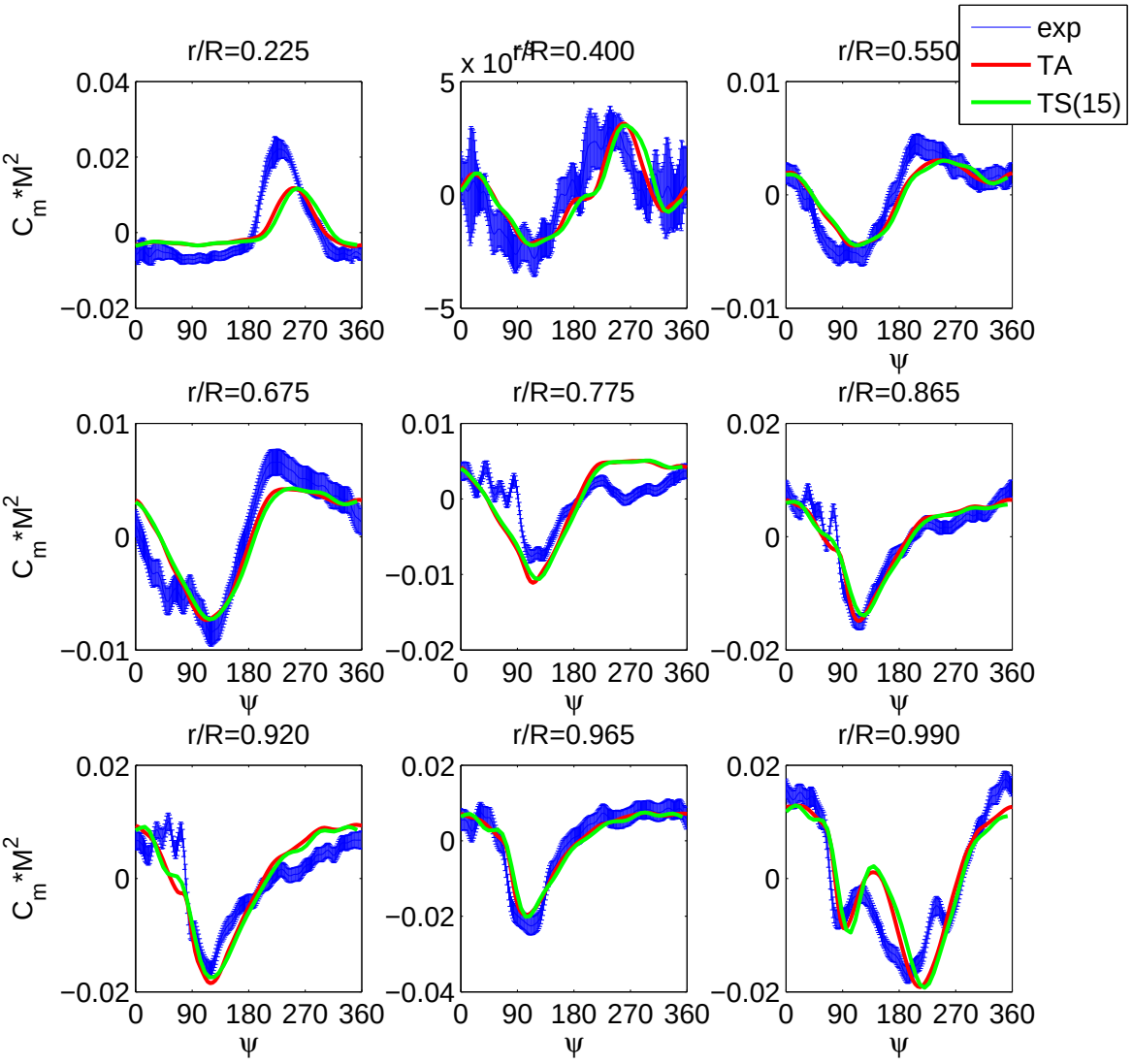

Figure 22. Section pitching moment of flight 8534 (four blade case (red-TA; green-TS)).

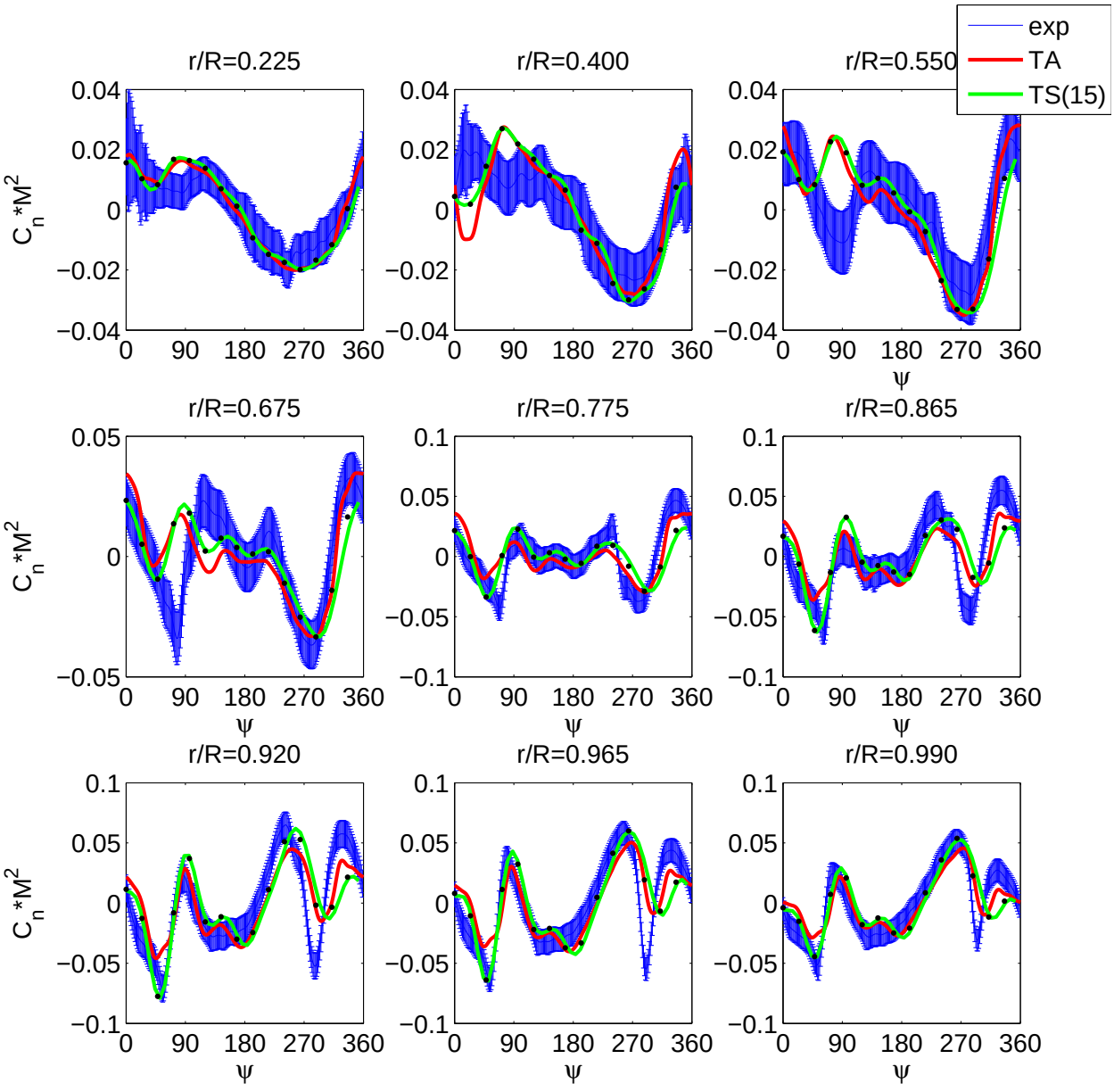

Figure 23. Section normal force of flight 8515 (four blade case (red-TA; green-TS)).

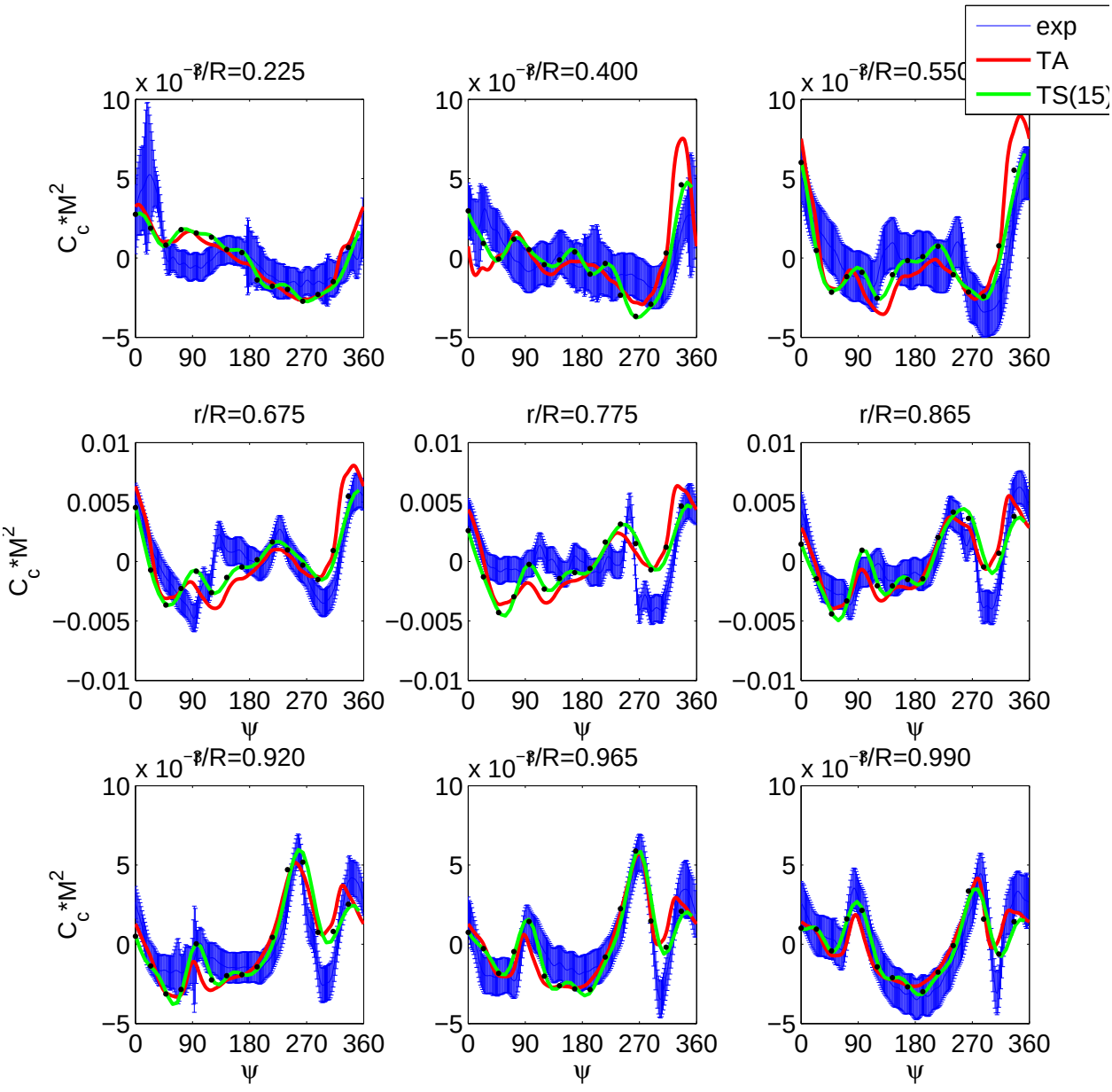

Figure 24. Section chord force of flight 8515 (four blade case (red-TA; green-TS)).

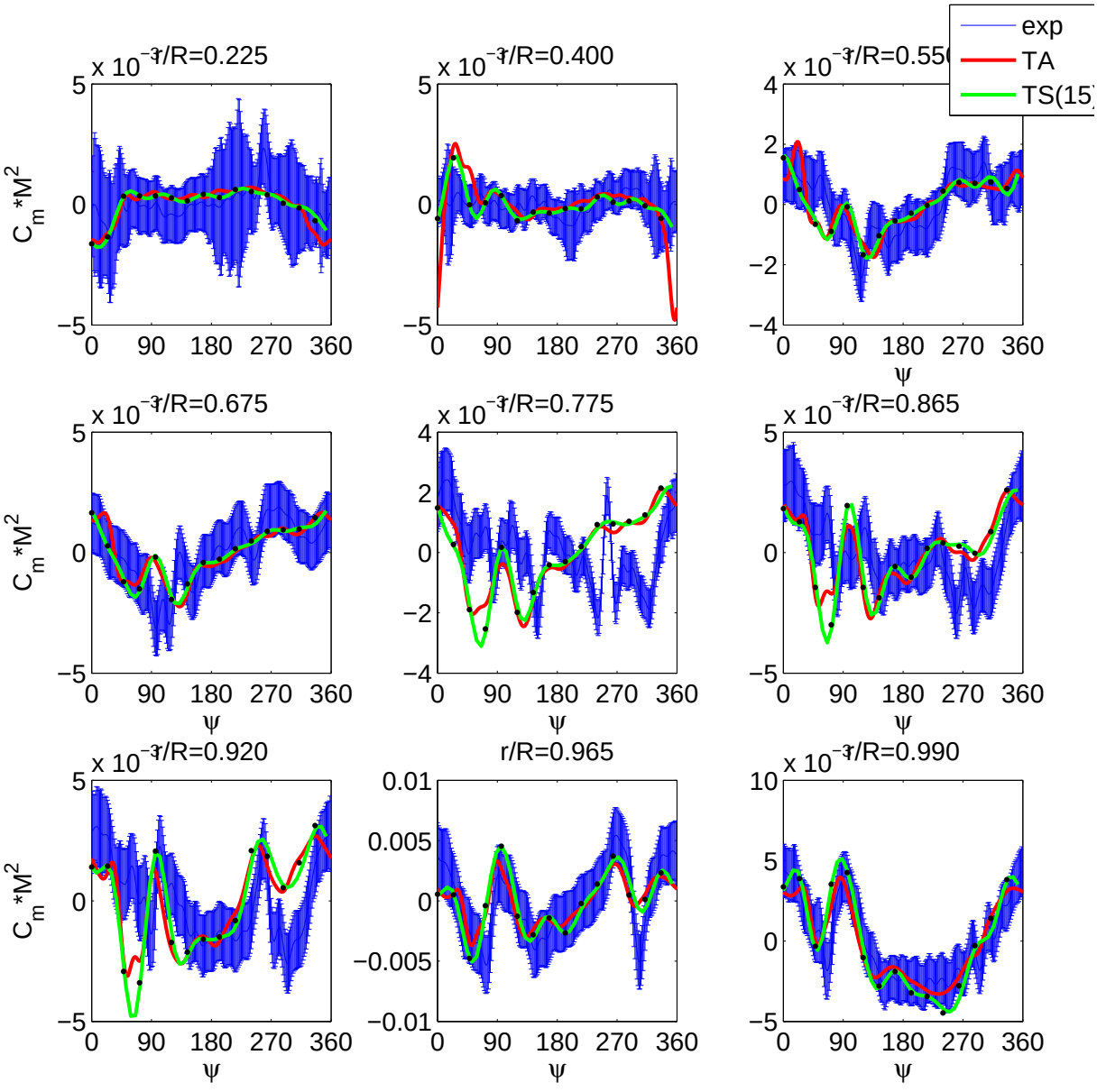

Figure 25. Section pitching moment of flight 8515 (four blade case (red-TA; green-TS)).

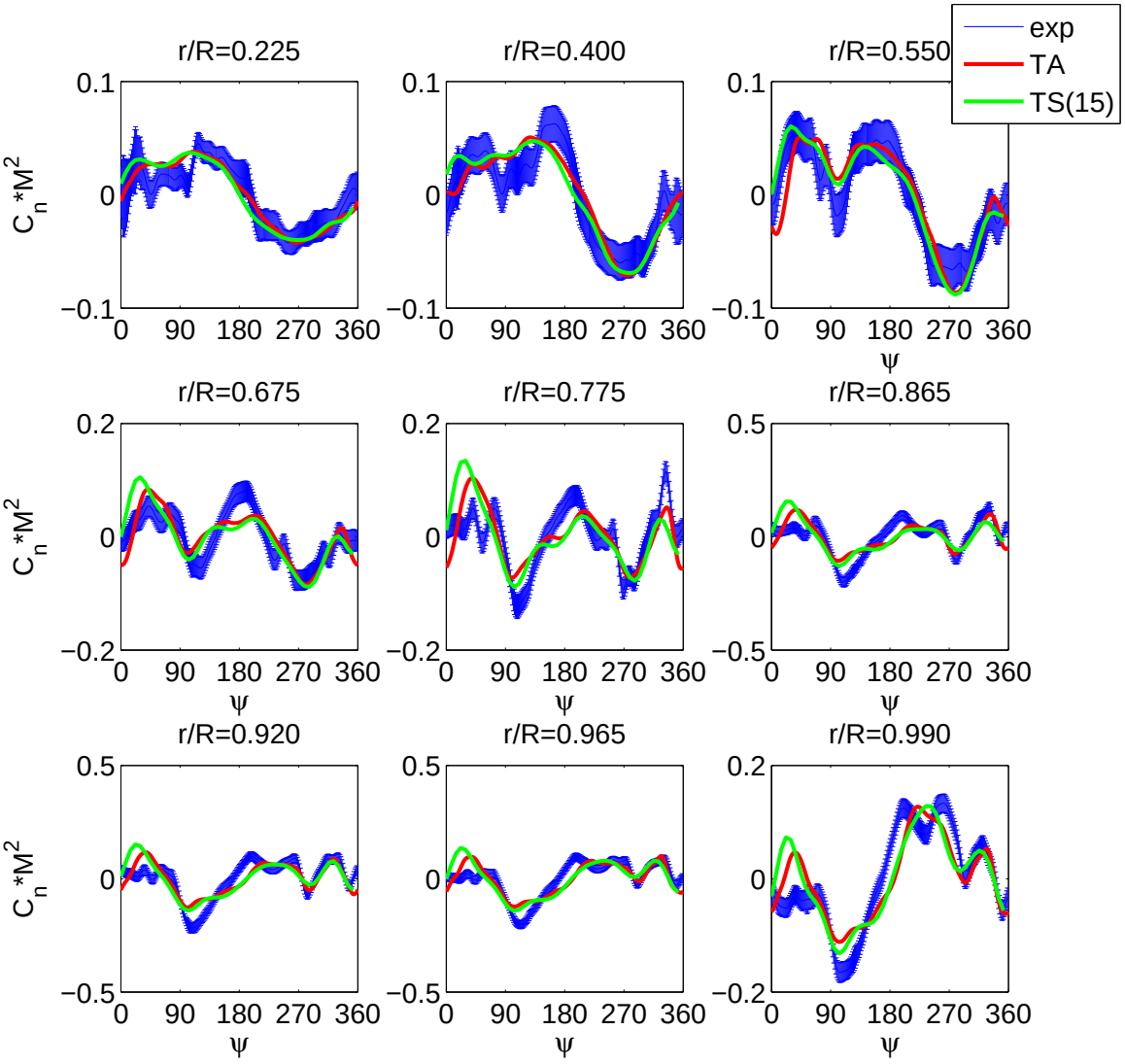

Figure 26. Section normal force of flight 9017 (red-TA; green-TS).

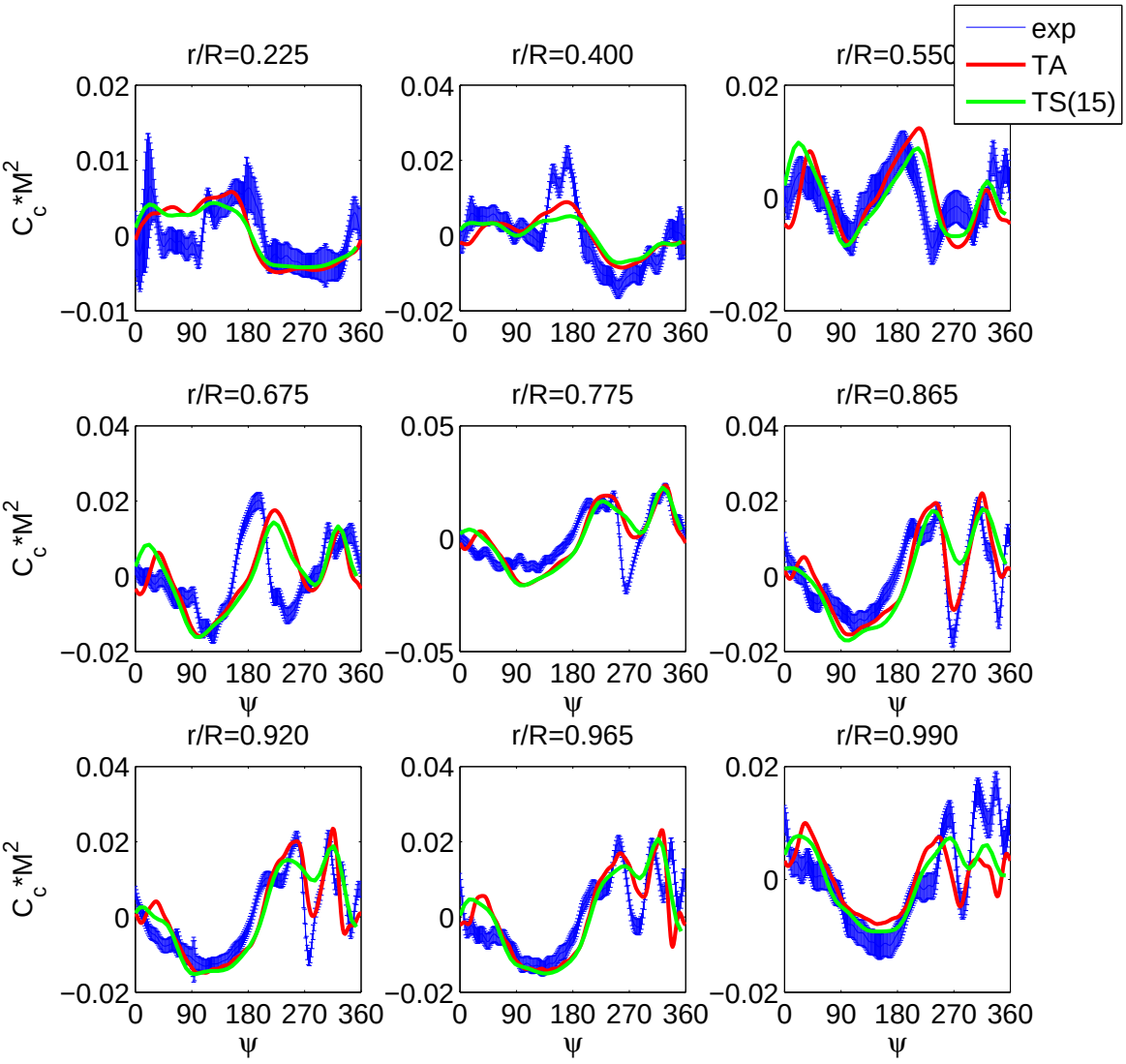

Figure 27. Section chord force of flight 9017 (red-TA; green-TS).

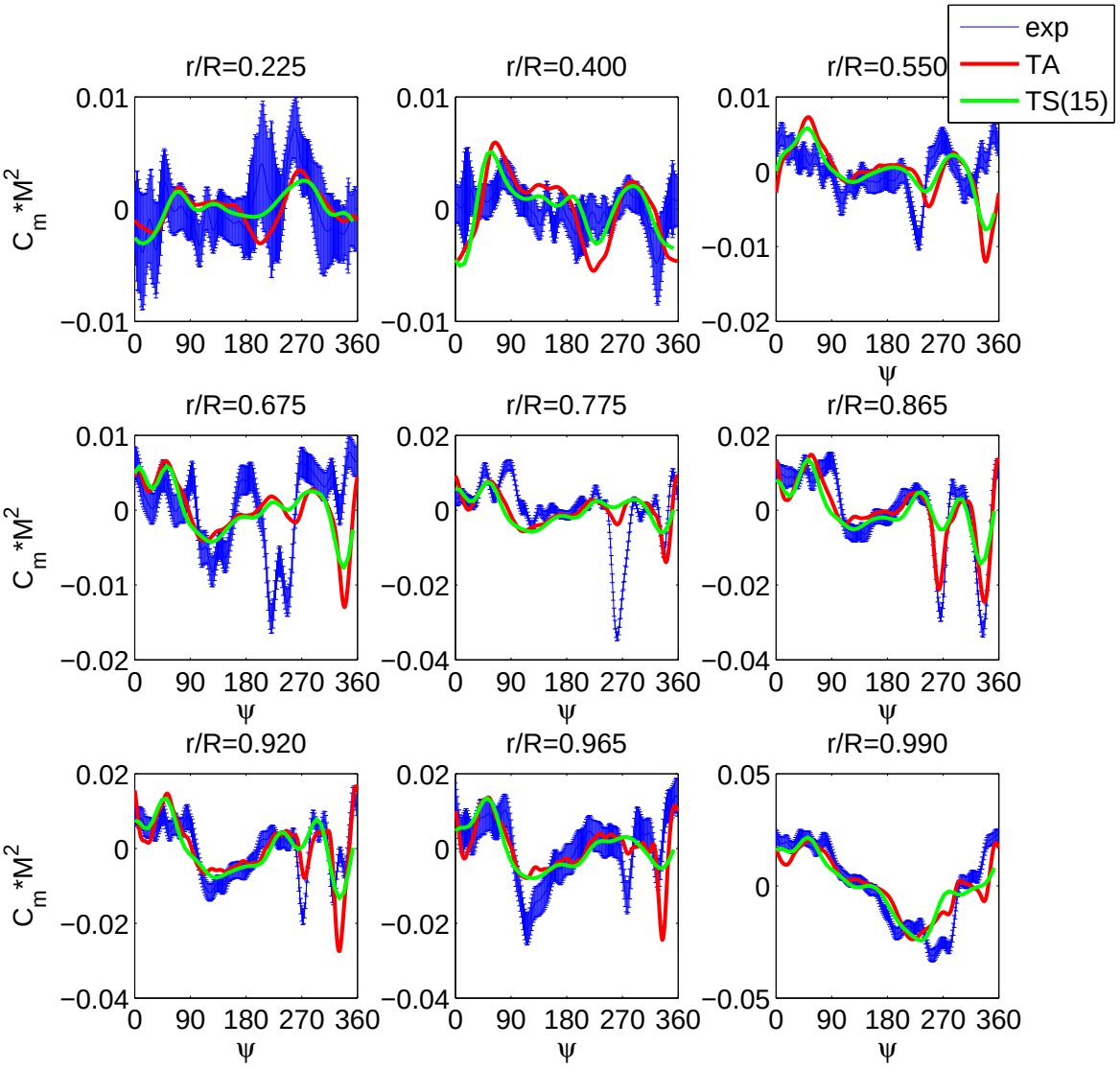

Figure 28. Section pitching moment of flight 9017 (red-TA; green-TS).